

# Formation and Evolution of Planetary Systems: Upper Limits to the Gas Mass in Disks Around Sun-like Stars

I. Pascucci<sup>1</sup>, U. Gorti<sup>2</sup>, D. Hollenbach<sup>3</sup>, J. Najita<sup>4</sup>, M. R. Meyer<sup>1</sup>, J. M. Carpenter<sup>5</sup>, L. A. Hillenbrand<sup>5</sup>, G. J. Herczeg<sup>5</sup>, D. L. Padgett<sup>5</sup>, E. E. Mamajek<sup>6</sup>, M. D. Silverstone<sup>1</sup>, W. M. Schlingman<sup>1</sup>, J. S. Kim<sup>1</sup>, E. B. Stobie<sup>1</sup>, J. Bouwman<sup>7</sup>, S. Wolf<sup>7</sup>, J. Rodmann<sup>7</sup>, D. C. Hines<sup>8</sup>, J. Lunine<sup>9</sup>, R. Malhotra<sup>9</sup>

## ABSTRACT

We have carried out a sensitive search for gas emission lines at infrared and millimeter wavelengths for a sample of 15 young sun-like stars selected from our dust disk survey with the *Spitzer Space Telescope*. We have used mid-infrared lines to trace the warm (300–100 K) gas in the inner disk and millimeter transitions of <sup>12</sup>CO to probe the cold (~20 K) outer disk. We report no gas line detections from our sample. Line flux upper limits are first converted to warm and cold gas mass limits using simple approximations allowing a direct comparison with values from the literature. We also present results from more sophisticated models following Gorti and Hollenbach (2004) which confirm and extend our simple analysis. These models show that the [S I] line at 25.23  $\mu\text{m}$  can set constraining limits on the gas surface density at the disk inner radius and traces disk regions up to a few AU. We find that none of the 15 systems have more than 0.04  $M_{\text{J}}$  of gas within a few AU from the disk inner radius for disk radii from 1 AU up to ~40 AU. These gas mass upper limits even in the 8 systems younger than ~30 Myr suggest that most of the gas is dispersed early. The gas mass upper limits in the 10–40 AU region, that is mainly traced by our CO data, are  $< 2 M_{\oplus}$ . If these systems are analogs of the Solar System, either they have already formed Uranus- and Neptune-like planets or they will not form them beyond 100 Myr. Finally, the gas surface density upper limits at 1 AU are smaller than 0.01% of the minimum mass solar nebula for most of the sources. If terrestrial planets form frequently and their orbits are circularized by gas, then circularization occurs early.

*Subject headings:* planetary systems: formation solar system: formation – circumstellar matter — infrared: stars

---

<sup>1</sup>Steward Observatory, The University of Arizona, Tucson, AZ 85721.

<sup>2</sup>University of California, Berkeley, CA 94720.

<sup>3</sup>NASA Ames Research Center, Moffett Field, CA 94035.

<sup>4</sup>National Optical Astronomy Observatory, Tucson, AZ 85719.

<sup>5</sup>California Institute of Technology, Pasadena, CA 91125.

<sup>6</sup>Harvard-Smithsonian Center for Astrophysics, Cambridge, MA 02138

<sup>7</sup>Max Planck Institute for Astronomy, Heidelberg, Germany.

<sup>8</sup>Space Science Institute, Boulder, CO 80301.

<sup>9</sup>Lunar Planetary Laboratory, The University of Ari-

## 1. Introduction

Circumstellar disks are a natural outcome of the star formation process (Shu et al. 1987). Initially massive and gas-dominated, they evolve into tenuous dusty disks possibly with embedded planets (e.g. Meyer et al. 2006). Studying the evolution of gas and dust in circumstellar disks is essential to understanding how planets form.

The properties of circumstellar dust have been extensively studied in young and old disks since the IRAS mission. The emerging evolutionary pic-

---

zона, Tucson, AZ 85721.

ture is of sub-micron interstellar grains that grow to larger sizes (up to km-size bodies) and settle to the disk midplane (e.g. Bouwman et al. 2001; Przygodda et al. 2003; Apai et al. 2005). In a later stage, collisions between forming planets and/or minor bodies such as asteroids or Kuiper Belt Objects can produce second-generation dust (or debris) in circumstellar disks (e.g. Rieke et al. 2005; Kim et al. 2005; Bryden et al. 2006). This evolution leads to tenuous dust disks where the emission from grains is optically thin to its own radiation. In contrast, less is known observationally about gas evolution in circumstellar disks.

The presence or absence of gas affects planet formation in profound ways. Gas masses between 1 and 10 times the dust masses in circumstellar disks control the dust dynamics and shape the disk structure (e.g. Takeuchi & Artymowicz 2001). The gas lifetime constrains the time for forming gas giant planets like Jupiter and Saturn. In addition, the ultimate size and distribution of giant planets may be affected by the disk gas mass. Even during the assembly of terrestrial planets, which concluded approximately 30 Myr after the origin of the Solar System (Jacobsen 2005), a few Earth masses of gas in the terrestrial planet region could have influenced the eccentricity and final size of growing planets (Kominami & Ida 2004).

Observations of gas have mainly targeted young accreting disks (few Myr old) and probed the cold outer regions (outside  $\sim 30$  AU) and the warm regions within  $\sim 1$  AU of such disks. Cold gas ( $20 \text{ K} < T < 50 \text{ K}$ ) is traced in the millimeter by CO rotational lines that indirectly measure gas masses in young accreting disks with radii of few hundred AU (e.g. Dutrey & Guilloteau 2004). The only bona-fide debris disk detected in millimeter CO transitions is that around the A star 49 Cet (Zuckerman et al. 1995; Dent et al. 2005). Warm gas ( $\sim 1000 \text{ K}$ ) in the inner disk ( $\leq 1 \text{ AU}$ ) is probed in the near-infrared by CO vibrational transitions (e.g. Najita et al. 2003). These transitions may also trace gas in the terrestrial planet zone of evolved tenuous disks. In addition,  $\text{H}_2$  rovibrational lines have been detected in a few disks and found to trace the surface layer of the disks at distances of 10–30 AU from the star (e.g. Bary et al. 2003). Observations in the ultraviolet have successfully detected a number of gas lines towards pre-main sequence stars (e.g. Valenti et al.

2000, 2003). In particular fluorescent  $\text{H}_2$  emission has been found tracing both warm gas ( $\sim 2500 \text{ K}$ ) at or near the disk surface within  $\sim 1 \text{ AU}$  from the star (Herczeg et al. 2002) as well as surrounding molecular gas shocked in the interaction with stellar outflows (e.g. Walter et al. 2003). These UV diagnostics are not sensitive to the bulk of the much colder gas at larger radii. This cold gas can be traced with  $\text{H}_2$  absorption lines in the FUV but only in optically thin disks that are observed close to edge-on. Stringent upper limits to the line-of-sight  $\text{H}_2$  column density through the edge-on disks of  $\beta$  Pic and AU Mic suggest that the primordial gas dispersed in less than 12 Myr in both systems (Lecavelier des Etangs et al. 2001; Roberge et al. 2005).

One region not adequately probed by most of the observations described above is the  $\sim 1 - 30$  AU region ( $\sim 300 - 50 \text{ K}$ ), corresponding to the giant planet forming region in the solar system. The Infrared Space Observatory (ISO) provided a first glimpse. Thi et al. (2001a) reported pure rotational  $\text{H}_2$  S(0) and S(1) line detections from a large number of pre-main sequence stars and also from three main-sequence stars with debris disks. These detections translated into large reservoirs of gas, suggesting a gas dispersal timescale longer than the accretion timescale. However, subsequent ground-based infrared spectroscopy (Richter et al. 2002; Sheret et al. 2003; Sako et al. 2005) and UV observations (Lecavelier des Etangs et al. 2001) cast doubt on whether the observed lines originated in disks.

As part of the Formation and Evolution of Planetary Systems (FEPS) *Spitzer* legacy program, we are carrying out a comprehensive survey of disks around Sun-like stars to characterize the gas dissipation timescale. In conjunction with this survey, Gorti & Hollenbach (2004, hereafter GH04) constructed detailed gas and dust models of optically thin dust disks in order to compare observational results with model spectra. In Hollenbach et al. 2005 (hereafter H05) we applied these models to FEPS observations of the disk around the 30 Myr star HD 105, and showed that less than  $1 M_{\text{J}}$  of gas exists in the planet-forming region (between 1–40 AU for a disk inner radius of  $\sim 1 \text{ AU}$ ). In the following, we extend our analysis to 15 sun-like stars surrounded by optically thin dust disks, most of which have ages in the range 5–100 Myr.

The target selection and observational strategy are presented in Sect. 2. From the non-detection of atomic and molecular gas lines, we place stringent upper limits on the gas mass in the planet-forming zone (Sect. 3 and 4). We discuss the implications on the gas evolution timescale and on the formation of gas giant and terrestrial planets in Sect. 5. Our findings are summarized in Sect. 6.

## 2. Observations and Data Reduction

In this Section we describe the target selection for our gas survey with *Spitzer* (Sect. 2.1) and the data reduction of the mid-infrared spectra (Sect. 2.2). In order to trace outer disk regions with gas colder than 50 K we complemented the *Spitzer* data of many sources with millimeter observations of  $^{12}\text{CO}$  lines (Sect. 2.3).

### 2.1. Target Selection and Observational Strategy

We selected objects from the FEPS dusty disk survey of 328 stars based on two observational criteria and several ancillary parameters. We chose the nearest objects with ages mostly between 5 and 100 Myr and those located in the lowest infrared backgrounds so that the observing time required to meet our goal would be minimized. Targets were chosen to span a range of infrared excess emission, X-ray luminosity, and spectral type (within the bounds of our program: 0.8–1.2  $M_{\odot}$ ). We required that mid- to far-IR excess be detected in IRAS and ISO observations and extended the sample to excess sources discovered within FEPS. We also included additional young sources ( $\leq 30$  Myr) lacking infrared excess emission. Here we focus on a subset of these sources, whose dusty disks are thin at optical wavelengths. Results on the optically thick dust disks will be reported in a future contribution. The properties of the optically thin sample are summarized in Table 1. Ten out of fifteen sources have excess emission from circumstellar dust starting at wavelengths longer than  $\sim 20 \mu\text{m}$ . Among the five sources with no excess emission, ScoPMS 214, AO Men, and V343 Nor were included in the sample because of their young ages ( $\leq 15$  Myr). Our MIPS and low-resolution IRS observations do not confirm the excess emission reported in the literature towards the older two sources HD 134319 and

HD 216803 (Spangler et al. 2001; Fajardo-Acosta et al. 1999). In the case of HD 134319, the ISO  $60 \mu\text{m}$  flux was contaminated by a nearby source detected in our MIPS 24 and  $70 \mu\text{m}$  exposures.

Our *Spitzer* IRS observations were designed to be sensitive to less than  $\sim 0.5 M_{\text{J}}$  in molecular hydrogen gas at a temperature of 100 K. Integration times were set to achieve a  $5\text{-}\sigma$  detection against the noise. We used the IRS high-resolution modules providing  $R \approx 700$  spectral resolution over 9.9–37.2  $\mu\text{m}$ . Note that the natural line-width of the gas is expected to be 10–100 times smaller than the  $\sim 430$  km/s resolution of the IRS high resolution spectra. The large wavelength coverage of the IRS on *Spitzer* enables us to probe various atomic and molecular lines in addition to the molecular hydrogen transitions. In fact, GH04 show that certain lines, such as [S I] at 25.23  $\mu\text{m}$  and [S II] at 34.8  $\mu\text{m}$ , are expected in many instances to be significantly stronger than the  $\text{H}_2$  lines.

### 2.2. Data Reduction of the High-resolution IRS Spectra

Observations of our 15 targets were obtained between September 2004 and August 2005. After our validation observations of HD 105 in December 2003, in which we obtained only single on-source exposures, we switched to an on-source/off-source observing strategy to better subtract the background and improve source extraction. The objects have been all observed in the Fixed Cluster-Offsets mode with two nod positions on-source (located at 1/3 and 2/3 of the slit length) and two additional sky measurements acquired just after the on-source exposures. The IRS or PCRS Peak-up options were used to place and hold the targets in the spectrograph slit with positional uncertainties always better than  $1''$  (1 sigma radial). We used the Short-High module (SH), covering the spectral range 9.9–19.6  $\mu\text{m}$ , and the Long-High module (LH) covering the wavelength range between 18.7 and 37.2  $\mu\text{m}$ . Both modules are cross-dispersed echelle spectrographs with spectral resolution of approximately 700. A summary of the observational log is given in Table 2. The plate scale of the detector is 2.3''/pixel for the SH module and 4.5''/pixel for the LH module. Emission at radii larger than  $\sim 50$  AU could be spatially resolved with the SH module for targets closer than 20 pc (see Table 1). However as we will show in

Sect. 4.2, mid-infrared lines only trace warm gas located within few AU from the disk inner radius. Such emission is spatially unresolved for all targeted disks.

Raw high-resolution IRS data were processed with the Spitzer Science Center (SSC) pipeline S12.02. We start our data reduction from the *droop* products. Corrections applied in the SSC pipeline at this stage include: saturation flagging, dark subtraction, linearity correction, cosmic ray rejection and integration ramp fitting. Further data reduction is based on self-developed IDL routines in combination with the SMART reduction package developed by the IRS Instrument Team at Cornell (Higdon et al. 2004). The first step consists of creating background subtracted images from sky measurements acquired after the on-source exposures<sup>1</sup>. Next we fix pixels marked bad in the "bmask" files with flag value equal to 2<sup>9</sup> or larger, thus including anomalous pixels due to cosmic-ray saturation early in the integration, or preflagged as unresponsive. The SSC provides additional hot pixel masks for individual campaigns/modules that include permanently as well as temporarily hot pixels. We correct for these hot pixels using the *irsclean* package provided by the SSC. The routines recognize if a pixel is marked in both the bmask and the additional hot pixel masks and correct only once. Bad and hot pixels are cleaned by averaging spatial profiles in rows above and below the affected row and then normalizing the average profile to that of the affected row. The profiles are fitted to the good data in the affected row by minimizing the  $\chi^2$ . These procedures have been extensively tested by the IRS GTO team and SSC<sup>2</sup>. We use the background subtracted pixel-corrected images to extract 1D spectra with the full aperture extraction routine in SMART.

We applied the same procedure to our sources and to calibrators observed within the *Spitzer* IRS Calibration program (PI, L. Armus). We used all the calibrators processed with the S12.0.2 pipeline (2 observations of HD 166780, 3 of HD 173511 and 1 of  $\xi$  Dra) to create two one-dimensional spectral response functions (one at each nod position) from

<sup>1</sup>Because we have the same RAMP and number of cycles for the source and the sky, we subtracted a sky exposure from each on-source exposure

<sup>2</sup><http://ssc.spitzer.caltech.edu/irs/roguepixels/>

the known stellar model atmosphere. The stellar models for the calibrators are available at the SSC web page<sup>3</sup>. The extracted spectra of each source are then divided by the spectral response function for each order and nod observation. The lower right corner of the chip is not well illuminated, resulting in a drop of signal at the end of each order. However, since the orders have a good overlap in wavelength, we simply trimmed the low-signal regions, retaining about 0.06  $\mu\text{m}$  overlap in the SH module and 0.1 micron in the LH module. After trimming, spectra over all slit positions and cycles are averaged on an order basis. The uncertainties at each wavelength are estimated by the 1 sigma standard deviations of the distribution of the data points used to calculate the mean spectrum over all cycles and nod positions, and thus indicate the repeatability of our measurements. To these uncertainties we included the error on the derived spectral response function by taking the standard deviation of the calibrator spectra divided by the stellar atmospheres. The error quoted at overlapping wavelengths is the error propagation of the mean value. An example of a reduced spectrum is shown in Fig. 1. All reduced spectra are available in the on-line article. We report no detection of gas lines in any of these IRS spectra. We find that a few anomalous pixels remain in the reduced spectra that were not flagged in the bmask nor in the hot pixel masks. These pixels are typically located at the beginning and/or at the end of a spectral order and not at the location of the expected gas lines (see for example the pixel at 27.78  $\mu\text{m}$  in Fig. 2).

### 2.3. Millimeter CO Observations and Data Reduction

Observations of <sup>12</sup>CO in J=2-1 (230.538 GHz) and J=3-2 (345.796 GHz) were obtained with the 10-m Submillimeter Telescope (SMT) during two campaigns, December-February 2003-2004 and December-January 2005-2006. The full-width-half-maximum (FWHM) beam size of the SMT observations is 33" and 22" for the J=2-1 and J=3-2 transitions respectively. The data were recorded using the CHIRP digital spectrometer (bandwidth of  $\sim$ 215 MHz and resolution of  $\sim$ 40 kHz)

<sup>3</sup><http://ssc.spitzer.caltech.edu/irs/calib/templ/>

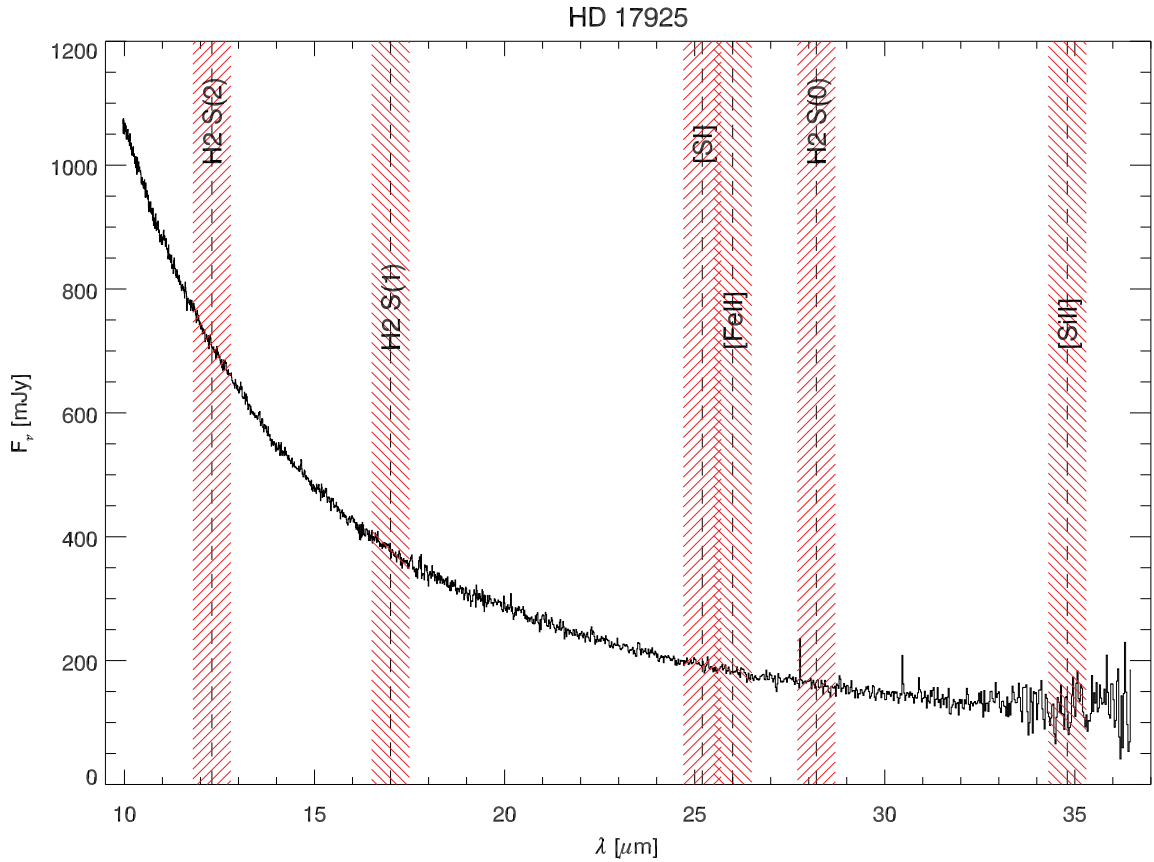


Fig. 1.— Spectrum of HD 17925 illustrating the location of the major molecular and atomic gas transitions (black dashed lines) covered by the IRS high-resolution modules. The hatched area (red in the electronic version) shows the region where we calculate the line flux upper limits (see Sect. 3.1 for more details). The continuum between 10 and 40  $\mu\text{m}$  is photospheric emission from HD 17925. Excess emission from dust was detected with ISO at 60  $\mu\text{m}$  (Habing et al. 2001 and Fig. 4). The reduced spectra of all targets discussed here are available in the on-line material.

and reduced using CLASS in the GILDAS<sup>4</sup> data reduction package. During data reduction, the spectra were smoothed to a velocity resolution of  $0.2 \text{ km s}^{-1}$ , about ten times smaller than the expected width of the line. A linear baseline was then removed from each spectrum, and all the spectra for a given source were coadded by weighting each spectra by  $\text{rms}^{-2}$ . We calibrated our temperatures by measuring the ratio of observed and expected emission lines from planets (the latter was computed with the ASTRO software within GILDAS). These ratios, also known as beam efficiencies, had mean values of 0.77 and 0.50 for the J=2-1 and J=3-2 during the first campaign and 0.74 and 0.55 for the J=2-1 and J=3-2 during the second campaign. Repeated observations of spectral line calibrator sources during each campaign indicate the dispersion in the calibration is 19%, and 28% for J=2-1 and J=3-2 respectively. This dispersion was not included in the estimates of the line flux upper limits in Sect. 3.2. For two FEPS sources (HD 37484 and ScoPMS 214), the heliocentric velocity was unknown at the time of the observations, and the spectrometer was centered on  $0.0 \text{ km/s}$ . The velocities were later determined from high resolution optical spectra (White et al. 2006), and in all three instances, the velocities were well within the spectrometer bandwidth ( $>100 \text{ km/s}$ ). We did not detect any CO emission line from any of our sources. The 1-sigma upper limits per channel are provided in Table 3. Values are given in the main beam scale, i.e. the antenna temperatures have been divided by the main beam efficiencies of the telescope at the specific frequencies.

### 3. Simple Estimates of Gas Mass Upper Limits

We have not detected any lines associated with the gas in our IRS spectra, nor in our millimeter data. Line flux upper limits can be compared to model predictions of line strength and provide stringent constraints on the amount of gas in the planet-forming region. We pursue rigorous theoretical comparisons in Sect. 4.2. Here for comparison to previous studies, we estimate gas mass upper limits in the approximation of optically thin emission at assumed fixed temperatures. Upper

limits to the warm and cold gas are derived from the  $\text{H}_2$  (Sect. 3.1) and CO non-detections respectively (Sect. 3.2). In addition, we calculate the upper limit on the radius of a putative gas disk under the assumption that the CO emission is optically thick in the inner regions (Sect. 3.2). This radius will be later compared to that derived from our detailed modeling of gas disks which satisfy the observed infrared line flux limits.

#### 3.1. Warm Gas Limits from $\text{H}_2$ Observations

To estimate line flux upper limits from the mid-infrared observations, we first extract a  $\pm 0.5 \mu\text{m}$  region around the expected feature. Then we fit a baseline using a first order polynomial. Five sigma upper limits to the line flux are derived by taking the local RMS dispersion of the pixels in the baseline subtracted spectrum over two pixels per resolution element, assuming the noise is uncorrelated. Note that because we calibrate our spectra from the average spectral response function of various standard stars, our upper limits partly include the error in the absolute flux calibration. We have tested that the line flux upper limits are not very sensitive to the width of the region where we fit the baseline. Choosing a region around the line that is  $0.5 \mu\text{m}$  smaller or larger than the  $1 \mu\text{m}$  width we adopt changes the upper limits on average by only 6%<sup>5</sup>. Our approach provides conservative upper limits. The use of a higher order polynomial to fit the continuum and/or the inclusion of the errors at each wavelength would lower the computed RMS and thus the line flux upper limits. Our RMS values are on average 20% higher than the error at the wavelengths of the expected lines. Table 4 summarizes the line flux upper limits for many of the transitions observed in the IRS modules:  $\text{H}_2$  S(2) at  $12.28 \mu\text{m}$ ,  $\text{H}_2$  S(1) at  $17.04 \mu\text{m}$ ,  $\text{H}_2$  S(0) at  $28.22 \mu\text{m}$ , [S I] at  $25.23 \mu\text{m}$ , [Fe II] at  $26.00 \mu\text{m}$ , and [Si II] at  $34.80 \mu\text{m}$ . We show examples of hypothetical  $5 \sigma$  lines in Fig. 2.

We convert  $\text{H}_2$  line flux upper limits into upper limits on the  $\text{H}_2$  mass (see e.g. Thi et al. 2001b for the equations) assuming that the gas

<sup>4</sup><http://www.iram.fr/IRAMFR/GILDAS>

<sup>5</sup>These tests have been made on the three lines that are the most informative when compared to the gas models: the  $\text{H}_2$  S(1) at  $17.04 \mu\text{m}$ , the [S I] at  $25.23 \mu\text{m}$ , and the [Fe II] at  $26.00 \mu\text{m}$

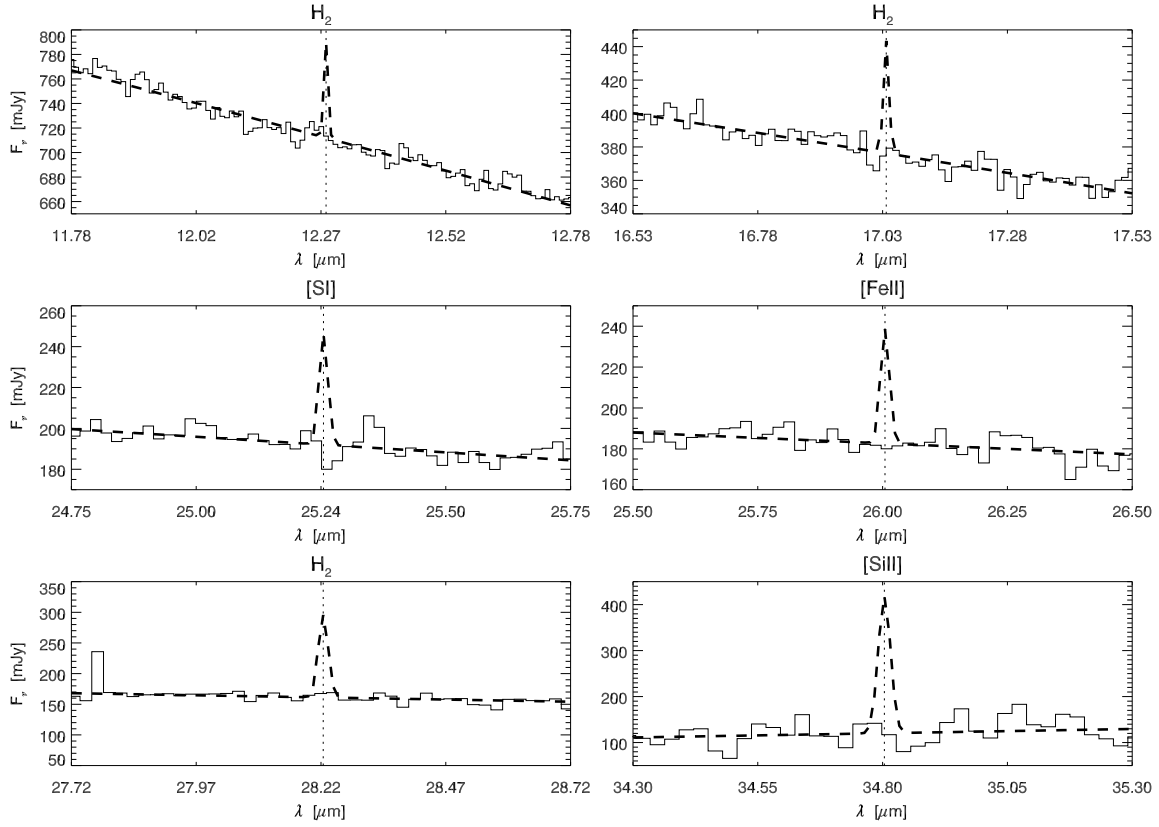


Fig. 2.— Expanded view of the wavelength regions around the expected lines toward the source HD 17925. Dashed lines are the hypothetical  $5\sigma$  line fluxes calculated assuming a resolution of 700 at all wavelengths. Lines are expected to be unresolved at all wavelengths. The pixel at  $27.78\mu\text{m}$  is an example of anomalous pixel that was not flagged in the bmask nor in the hot pixel masks.

is in local thermal equilibrium, that the H<sub>2</sub> lines are optically thin, and that the gas temperature is 100, 150 or 200 K. Temperatures of  $\approx 100$  K correspond to the gas from which our own Jupiter and Saturn are thought to have formed (e.g. Gautier et al. 2001). Expanding the temperature range to 200 K allows us to make a direct comparison with published gas masses and upper limits for circumstellar disks (e.g. Thi et al. 2001b; Sako et al. 2005; Chen 2005; H05; Chen et al. 2006) and illustrate how gas masses depend on the assumed gas temperature. The H<sub>2</sub> S(2) line does not set stringent limits for temperatures lower than  $\sim 300$  K, the H<sub>2</sub> S(1) transition is the most sensitive line at 150 and 200 K, while the H<sub>2</sub> S(0) and the H<sub>2</sub> S(1) transitions provide similar values for gas at 100 K. In Table 5 we report the lowest gas mass upper limits for temperatures of 100, 150, and 200 K and indicate whether they are derived from the H<sub>2</sub> S(0) or the H<sub>2</sub> S(1) transitions for gas at 100 K. This simple approach shows that gas masses are very sensitive to the assumed gas temperature: if the emitting gas is as cold as 100 K it takes about hundred times more mass to produce the measured line flux upper limits than if gas is at 200 K. Hence, it is very important to utilize detailed disk thermal models which describe the gas density and temperature distribution and which predict line fluxes from disks of a given mass for comparison with the observed upper limits on line fluxes.

Our measurements for optically thin disks are more sensitive than the ISO observations by Thi et al. (2001b) by at least a factor of 4 for sources at similar distance. The line detections claimed by Thi et al. suggested that relatively large amounts (6.7-0.2  $M_J$ ) of gas can persist into the debris-disk phase. Our gas mass upper limits show that even the six youngest disks in our sample (5-20 Myr) have less than 0.6 Jupiter masses of 100 K gas (or less than 0.005 Jupiter masses of 200 K gas). Our results are in agreement with the recent findings by Chen (2005) who reports masses of 100 K gas smaller than  $15M_\oplus$  (or  $0.05 M_J$ ) in the disks of  $\beta$  Pictoris ( $\sim 12$  Myr, Zuckerman et al. 2001) and 49 Ceti ( $\sim 10$  Myr, Zuckerman et al. 1995). These low gas masses argue for short gas dispersal timescales.

Gas masses in Table 5 are provided mainly for comparison to previous studies. More detailed

modeling of the dust and gas components is necessary to understand the mechanisms relevant to the gas heating, to determine gas temperatures, and thus infer total gas masses from our non-detections. This procedure has been fully explored in H05 for HD 105, one of the first sources in the FEPS gas program, and is extended to our larger sample in Sect. 4.

### 3.2. Cold Gas Limits from CO Observations

For the millimeter observations, we convert the 1-sigma noise into line flux upper limits as follows:

$$\Delta F(\nu) = \frac{2k\Delta T_{\text{rms}}}{\lambda^2} \times \frac{\pi\theta^2}{4} \times d\nu \times \sqrt{N} \quad (1)$$

where  $k$  is the Boltzmann constant,  $\Delta T_{\text{rms}}$  are our 1-sigma upper limits per channel as reported in Table 3,  $\theta$  is the beam in radians at the transition  $\lambda$ ,  $d\nu$  is the frequency resolution ( $d\nu = 0.2$  km/s), and  $N$  is the number of channels on which the line is distributed. Assuming a line width of 5 km/s, which is the Keplerian velocity for gas at  $\sim 30$  AU around a solar mass star, we have 25 channels for the SMT resolution of 0.2 km/s. The 5-sigma line flux upper limits are summarized in Table 6 and will be used here to provide an upper limit either to the CO mass in disks optically thin to the CO transitions or to the size of an optically thick CO disk. We will use our gas models to fully characterize the CO emission in Sect. 4.2.

Assuming that CO is optically thin throughout the disk, we can convert our line flux upper limits into CO mass upper limits. We use the formulation of Scoville et al. (1986) with appropriate changes to take into account different CO transitions and adopt an excitation temperature of 20 K. We note that the CO mass is not very sensitive to the gas temperature and changes only by  $\sim 20\%$  if we assumed an excitation temperature of 40 K. Five-sigma upper limits to the CO mass are summarized in Table 6. Our limiting values are typically a factor of 10 higher than those reported by Najita & Williams (2005) for the disks around HD 104860 and HD 107146, due to a combination of shorter integration times and the assumption of larger line widths. Still these upper limits convert to less than a few  $M_\oplus$  of total gas mass for many sources assuming the interstellar H<sub>2</sub>/CO number



ratio of  $10^4$ . However, there are at least two important issues that need to be considered: the possible condensation of CO onto grains and the photodissociation of CO molecules. Both these processes reduce the CO gas phase abundance relative to H and thereby raise the upper limit on the total mass. Condensation of CO occurs for grain temperatures  $\leq 50$  K depending on the substrate onto which CO is adsorbed (see e.g. Najita & Williams 2005 for a discussion). The lack of submillimeter continuum data for our sample does not allow us to constrain the temperature of the cold grains, and thereby to estimate the effect of CO condensation. However, we will show in Sect. 4 that photodissociation is a severe problem for tenuous gas disks such as those we have observed. If CO is optically thin but much of the gas phase carbon is found in  $C^+$  or C, then the CO gas we detect would be representative of only a small fraction of the total gas mass, and the total gas mass associated with the optically thin CO could be  $\gg$  few  $M_{\oplus}$ . In addition, the optically thin limits on CO mass tell us nothing about the CO mass located in the optically thick inner regions.

Assuming the existence of such an optically thick inner disk (which is indeed present in young accreting disks, Dutrey et al. 2004), we can set limits to the disk size by our CO flux upper limits. For simplicity we describe the CO emission as that from a blackbody times the solid angle subtended by a face-on disk<sup>6</sup> and compare this emission to our 5-sigma line flux upper limits. Table 6 summarizes the inferred upper limits on optically thick disk radii for a black body temperature of 20 K. Disk radii are more sensitive to the assumed blackbody temperature than disk masses: a blackbody temperature of 40 K results in  $\sim 35\%$  smaller radii than those reported in Table 6. It is important to characterize the region inside which optically thick CO gas could exist because inside that region, gas masses could be high and still be undetected in CO. It is in these regions that the infrared upper limits may constrain the mass or surface density. In Section 4 we will compare these radii, calculated

<sup>6</sup>Because we do not have information on the disk inclinations, we assume face-on configurations here and in the following gas models. For optically thick lines the observed flux is proportional to the projected area of the disk. Thus, fluxes from optically thick lines can be corrected by multiplication with the cosine of the disk inclination.

for constant T, with those inferred by detailed gas models which compute the radial and vertical dependence of T and the detailed radiative transfer operating for the CO transitions as well as for the infrared transitions.

#### 4. Constraining the Gas Mass in the Planet-forming Zone

Even though  $H_2$  is the dominant constituent of the gas,  $H_2$  lines are not always the strongest transitions from circumstellar disks. Depending on the density, temperature and chemical structure (which in turn depends on the radiation field and disk surface density distribution), other infrared atomic and molecular lines can have higher luminosities (GH04). In this section, we make use of the line flux upper limits derived from the mid-infrared and mm CO transitions to derive constraining upper limits for the gas mass in the planet-forming zone.

Hollenbach et al. (2005) have shown that the dust disk of HD 105 is so tenuous that the dust does not affect the gas temperature or gas disk structure. In Sect. 4.1 we demonstrate that our systems also have too low dust surface density for gas-grain collisions to heat or cool the gas. Gas heating in these tenuous disks is dominated by X-rays and UV radiation from the central star, and therefore we can ignore the dust component in modeling the gas emission (Sect. 4.2). This is completely opposite to the case for young optically thick disks, where the gas temperature in much of the disk is coupled to the dust temperature by collisions, and where the surface gas is heated by the grain photoelectric heating mechanism (e.g. Jonkheid et al. 2004).

##### 4.1. Gas-dust Collisions versus X-ray Heating

To understand whether dust may be an important heating mechanism for the gas, we need to evaluate the dust surface density of our disks. The observed infrared continuum excess from a disk gives an upper limit to the dust surface density for a chosen grain size. Ten of our gas sources have infrared excess emission at wavelengths longer than  $\sim 20 \mu\text{m}$  with spectral energy distributions (SEDs) characteristic of optically thin dust disks (see Fig. 3 and 4). We use HD 37484 and its

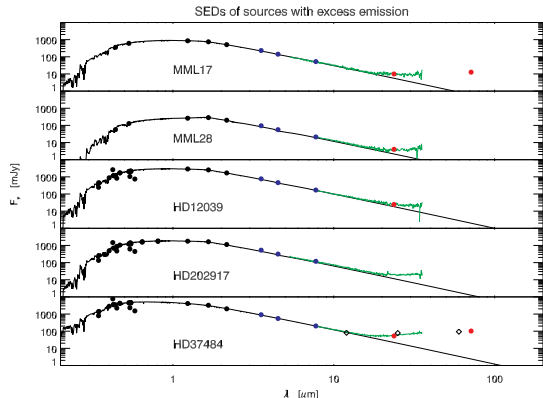


Fig. 3.— Spectral energy distributions (SEDs) of sources with excess emission. Blue, red and black filled-circles are IRAC, MIPS and ground-based data points. Green lines are IRS low resolution spectra. IRAS and ISO measurements are in diamonds and squares respectively. Kurucz model atmospheres are overplotted with black lines.

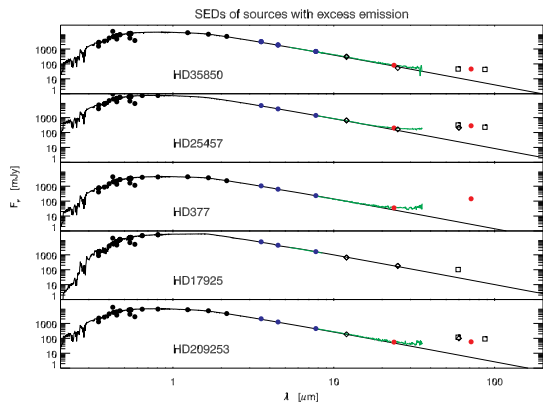


Fig. 4.— SEDs of sources with excess emission. See Fig. 3 for the plotting symbols.

disk as our demonstrative case because the system has the largest warm excess emission and the star has a low X-ray luminosity, thus representing the case with the largest dust surface density and the lowest X-ray heating of the gas. We assume that the disk has a dust surface density proportional to  $r^{-1}$  (e.g. the Vega best fit model to its debris disk by Su et al. 2005). We estimate in three steps the maximum dust surface density at the disk inner radius that is consistent with the infrared observations: i) we calculate the dust temperature using the analytical solution of the radiative transfer equation for optically thin disks (e.g. Pascucci et al. 2004, eq. 5); ii) we determine the excess emission by subtracting the best-fit Kurucz model atmosphere from the observed data; iii) we write the dust re-emission in terms of the dust surface density at the inner radius (e.g. Wyatt et al. 1999 eq. 3) and require that the re-emission does not exceed the observed excess at any wavelength. The maximum dust surface density for inner radii from 1 to 19 AU is shown in Fig. 5 for a disk with small ( $0.2 \mu\text{m}$ ) and large ( $2 \mu\text{m}$ ) grains. The dust surface density for small grains is lower than that for large grains at all disk radii. This is because smaller grains are warmer than larger ones at the same distance from the star and because, for the same dust surface density, smaller grains have more total surface area than larger grains.

On the other hand, a lower limit to the dust surface density is obtained if the dust is to dominate the heating by X rays. Heating from gas-dust collisions is proportional to the product of the densities of dust and gas while X-ray heating is only proportional to the density of gas. By equating the contribution from gas-dust collisional heating and X-ray heating (see GH05 for the analytic forms of these heating processes), we obtain a minimum dust density for dust-gas collisions to contribute as much as X-ray heating. We compare the two heating mechanisms at the midplane of the disk where the number density is highest at any given radius, and hence where collisional heating is maximum. This is also the region where X-ray heating is at its lowest, since the attenuation is highest. To convert the number density to surface density we use the mass of spherical Draine & Lee silicate grains and a disk scale height of 0.1 times the radial distance, which is a good approximation for the inner regions of flared disks (e.g. Chiang &

Goldreich 1997). The resulting minimum dust surface densities for different inner disk radii and for two grain sizes are summarized in Fig. 5. These values are obtained for a gas temperature of 70 K. Note that the general trend will not change if a different gas temperature is assumed, but for gas hotter than the dust at any radius gas-dust collisions will result in cooling rather than heating the gas. However, the magnitude of the collisional cooling is similar to the magnitude of the collisional heating, the energy transfer being proportional to  $(T_{\text{gas}} - T_{\text{dust}})$ .

The comparison of the two surface densities proves that our dust disks are too tenuous for dust to appreciably affect gas heating or cooling. This simple approach shows that at least two orders of magnitude higher dust surface densities are necessary for dust-gas collisions to equal X-ray heating. Because the other gas sources have lower excess emission than HD 37484 and/or higher X-ray luminosities, this result extends to the entire sample. We also point out that grain photoelectric heating is completely negligible for optically thin dust disks where most of the dust grains have grown to sizes larger than the very small ( $\ll 0.2 \mu\text{m}$ ) interstellar grains which dominate grain photoelectric heating (see the case of HD 105 by H05 and Fig. 3 by GH04). We therefore proceed to model the gas temperature and density structure of disks ignoring their dust properties.

#### 4.2. Gas Models for Optically Thin Disks

The simple approximations adopted in Sections 3.1 and 3.2 allowed us to obtain initial estimates of gas mass upper limits and compare them to values published in the literature. The upper limits were shown to depend strongly on the assumed gas temperature. We can improve on these estimates by applying comprehensive gas models to calculate the gas disk temperature and thus infer *total* gas mass upper limits for the targeted disks. We use the models of GH04 that include the chemistry and thermal balance in a self-consistent manner and calculate the vertical density structure and the temperature in the radial and vertical directions. These models include heating and cooling from gas-dust collisions, stellar and interstellar UV radiation, stellar X-rays, collisional deexcitation of vibrationally excited  $\text{H}_2$  molecules, grain photoelectric heating, exothermic

chemical processes, and cosmic rays. Condensation of molecules onto grains is not implemented for two main reasons. First, infrared lines originate from regions where dust is too hot ( $\geq 100 \text{ K}$ ) for condensation to occur appreciably. Second, the code is steady state but would require time dependent solutions to properly treat the condensation of molecules. Gas-phase species are assumed to have interstellar abundances (Savage & Sembach 1996 and Appendix A in GH04). We demonstrated in Section 4.1 that gas-dust collisions and grain photoelectric heating are insignificant heating and cooling mechanisms in tenuous dust disks and therefore we removed the dust component in the models that follow.

**FIDUCIAL DISK MODEL.** We first consider a fiducial face-on gas disk extending from 1 to 100 AU with a surface density dependence of  $\Sigma \propto r^{-1}$ , as indicated from observations of young disks (e.g. Dutrey et al. 1996). The main input parameters to the gas models are the stellar properties reported in Table 1 and stellar FUV fluxes (UV fluxes between  $6 \text{ eV} < h\nu < 13.6 \text{ eV}$ ). Our first modeling of the disk around HD 105 showed that stellar X ray and UV photons dominate the gas heating in tenuous dust disks (the UV heats not by the grain photoelectric heating mechanism but by pumping  $\text{H}_2$  and by photodissociating and photoionizing molecules and atoms, H05). Because stellar X-ray and UV fluxes depend on the stellar activity, we tried to collect measurements for each source. X-ray data are available for all targets (see Table 1) while only 5 of our sources have been observed in the UV by the International Ultraviolet Explorer (IUE). For these sources we merged the IUE data with the Kurucz model atmospheres<sup>7</sup> and estimated the flux in 8 energy bins (from 0.7 to 13.6 eV) that are relevant for the photodissociation and photoionization of dominant atomic and molecular species like S, Fe, Mg, Si, CO and  $\text{H}_2$ . Where we lack UV data for our targets, we searched for stars with similar spectral type, age, and colors in the IUE archive and used them as templates for the FUV flux. For sources where ages are not well-determined we used the spectral

<sup>7</sup>The Kurucz model atmospheres for the stellar parameters in Table 1 match in all cases the long wavelength IUE data (from  $\sim 3000 \text{ \AA}$ ). We used the IUE data for wavelengths  $< 3000 \text{ \AA}$  and the Kurucz model atmospheres for longer wavelengths.

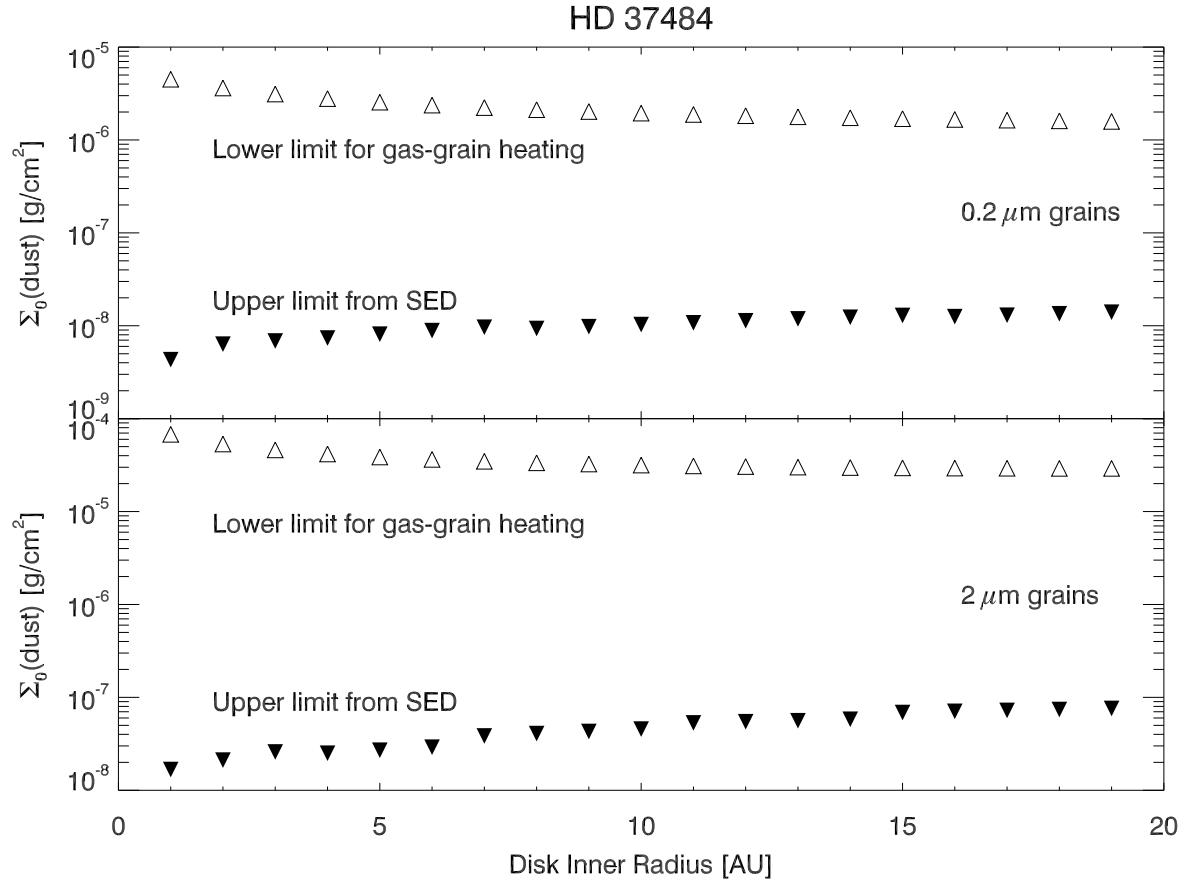


Fig. 5.— Comparison of dust surface densities at different disk inner radii for the source HD 37484. Open triangles indicate the minimum surface density for dust to contribute as much as X-rays in heating the gas at 70 K. Upside down filled triangles are the surface density upper limits imposed by the observed excess emission. For the dust, we adopted silicate grains with two sizes (0.2 and 2  $\mu\text{m}$ ) and opacities from Draine & Lee (1984). Note that there are at least two orders of magnitude between the limits inferred from the SED modeling and from gas–grain heating at any disk inner radius. This shows that gas–grain collisions are an insignificant heating source in these tenuous dust disks. They also cannot dominate the cooling of the X-ray heated gas (see text).

type and X-ray luminosity as the main criteria for assigning templates. We estimated the H I Ly-alpha flux from the X-ray flux, based on the empirical relationship by Wood et al. (2005). Since Ly-alpha emission contributes most of the FUV emission from late-type stars, we use it as a proxy for the total FUV emission and scale the templates accordingly, yielding order-of-magnitude estimates for the stellar UV field. A summary of UV templates and luminosities is given in Table 7. In Sect. 4.3 we will discuss the dependence of our results on the input parameters that are most uncertain: the disk inner radius, the surface density slope, and the stellar UV luminosity.

**METHOD.** We calculate the line fluxes from gas models with the total disk mass as our main variable parameter. For each transition reported in Tables 4 and 6, we find a disk mass where the calculated line flux from the models matches the observed flux limit. We determine the radius,  $R_{\text{em}}$ , from within which 90% of the emission originates for each transition and also define a disk mass associated with this region  $M_{\text{em}}$ , which includes mass from the inner radius to  $R_{\text{em}}$ . We also calculate the radius  $R_{\text{thick}}$  within which the CO emission is optically thick. This region corresponds to a vertical column density of CO molecules of  $10^{15} - 10^{16} \text{ cm}^{-2}$  (this value is similar for the two CO lines and corresponds to line optical depths larger than 1). Our modeling results are summarized in Tables 8 and 9.

**RESULTS FROM THE MID-INFRARED LINES.** We find that the [S I] transition at  $25.23 \mu\text{m}$  sets the most stringent upper limits on the gas mass in comparison to the limits set by the other mid-infrared lines. We explored the sensitivity of our results to the S abundance in the gas phase using the disk of HD 35850 as a test case. Observations from comet Halley dust suggest that about half of the S could be in FeS grains (e.g. Pollack et al. 1994). Some S could be removed from the gas phase component of circumstellar disks in this way, as recently proposed by Keller et al. (2002). However, current observations cannot quantify the amount of S into grains. To investigate a pessimistic case we reduced the S abundance in gas phase by 90%. This reduction results in a 5 times larger gas mass upper limit. This is because for such a low mass disk the [S I] line is nearly optically thin (optical depths of 2-3),

so that the [S I] flux drops nearly proportional to the gas mass. Note that even if [S I] upper limits would be increased by a factor of 5, they would still be more stringent than those inferred from H<sub>2</sub> lines for most of the sources (see below).

Our gas models predict also relatively strong [Si II] lines at  $34.8 \mu\text{m}$ , however the IRS spectra become noisier at longer wavelengths and our line flux upper limits are not as low. These results are in agreement with what we found for the disk around HD 105 (H05). The [Fe II] line at  $26 \mu\text{m}$  is the second most sensitive transition and can set useful gas mass upper limits for two-thirds of the sample (in other words, in one-third of the sample, our models did not produce detectable [Fe II] no matter how much gas mass was contained within the disk). The H<sub>2</sub> S(1) line at  $17 \mu\text{m}$  provides the most stringent upper limits when compared to the other two H<sub>2</sub> lines; nevertheless gas masses can be constrained only for one-third of the sample with this diagnostic. This is because the transition probabilities of the H<sub>2</sub> lines are orders of magnitudes smaller than those of the [S I] and [Fe II] transitions while their excitation temperatures are quite similar. The H<sub>2</sub> surface density upper limits are typically a factor of 10 higher than the surface densities set by [S I], while the [Fe II] transitions provide values similar to those from [S I] for many sources.

For an inner disk radius of 1 AU, the models indicate that the emitting region for the mid-infrared transitions is typically a few AU and extends up to  $\sim 5$  AU in a few of our fiducial disks, suggesting that we are tracing a region analogous to that between Earth and Jupiter in our Solar System. We note that the gas mass upper limits inferred from modeling the [S I] lines are less than  $0.4 M_{\oplus}$  in the 1-5 AU region for all sources and are as low as a tenth of an Earth mass for two-thirds of the sample.

Comparing gas masses from the models to the simple LTE approximation (Sect. 3.1) requires knowing the characteristic temperature of the emitting gas. For the 5 sources where we could set limits from the H<sub>2</sub> S(1) line, we computed mean temperatures as follows:

$$\langle T \rangle = \sum F_i \times T_i / \sum F_i ,$$

where the sum is carried out over the spatial grid and the flux is the H<sub>2</sub> S(1) flux. We obtain mean

temperatures between 230 K (for HD 35850) and 160 K (for HD 216803). This temperature range reflects the different source heating; K-type stars like HD 17925 should have even lower  $\langle T \rangle$  close to 100 K. Limits on the mass of the emitting gas from modeling the [S I] line ( $M_{\text{em}}$  in Table 8) are typically a factor of 50 and of 10 lower than the warm gas limits calculated in Sect. 3.1 for gas temperatures of 150 K and 200 K respectively. The difference results from the use of [S I] as the tracer and the temperature structure in real disks. The limits on the *total* gas mass in a disk depends on the power law of the gas surface density and on the outer disk radius. For our fiducial disk model ( $\Sigma \propto r^{-1}$ ,  $1 \leq r \leq 100$  AU) upper limits to the total gas mass range from  $10 M_{\oplus}$  (for ScoPMS 214) to  $0.5 M_{\oplus}$  (for HD 17925), with higher limits typically for the more distant sources, which are also the younger (see last column of Table 8).

**RESULTS FROM THE MILLIMETER CO LINES.** While mid-infrared line luminosities trace the inner few AU of circumstellar disks, millimeter CO transitions are sensitive to colder gas located in the outer disks. CO is mainly heated by stellar X-ray and UV emission, but at large disk radii ( $\sim 20$  AU for a star with  $L_{\text{UV}} \sim 10^{-3} L_{\odot}$ ) the interstellar UV field can dominate the local stellar UV. Fig. 6 shows the line luminosity per logarithmic radial annulus produced in a disk as a function of  $r$ . Mid-infrared line luminosities increase steeply at the disk inner radius, peak in the inner few AU, and rapidly fall as the temperature decreases. In contrast, CO line luminosities gradually increase with radius, peak at larger disk radii, and decline as CO begins to photodissociate. CO emission is so widespread that radii as large as 20 AU and up to 60 AU (see  $R_{\text{em}}$  of Table 9) are required to encompass 90% of the CO luminosity. This emission is mostly optically thick, suggesting that as a first approximation CO is mainly tracing the radius inside of which the CO is optically thick rather than the total disk mass. The disk radii estimated with the simple assumption of optically thick CO emission and 20 K temperature are typically a factor of 2 higher (and can be up to a factor of 4 higher, e.g. HD 12039) than the  $R_{\text{thick}}$  from the models. This suggests that gas temperatures as high as  $\sim 50$  K are more representative of the region where CO is optically thick (see also the discussion in Sect. 3.2). In the case of

HD 17925 the low observed flux limits only allow a very tenuous gas disk. The low column density of the disk results in photodissociation of CO by the interstellar UV field (the average  $\text{H}_2/\text{CO}$  number ratio is  $10^5$ , an order of magnitude higher than the interstellar value) and CO emission from this disk is optically thin at all radii.

### 4.3. Dependence of the Results on Uncertain Input Parameters

In this section we test the dependence of our results on the slope of the gas surface density, on the stellar UV field, and on the disk inner radius, that are the main input parameters to our gas models lacking independent observational constraints.

First, we consider different slopes of the gas surface density power-law,  $\Sigma(r) \propto r^{-\alpha}$ , and use the disk around HD 35850 as the demonstrative case. In addition to our fiducial disk model with  $\alpha = 1$ , we summarize in Fig. 7 results for a flatter ( $\alpha = 0.5$ ) and a steeper ( $\alpha = 1.5$ ) surface density distribution, thus comprising the observed range of surface density slopes in circumstellar disks. For a disk with fixed mass, distributing more mass in the inner regions ( $\alpha = 1.5$ ) results in increased mid-infrared line luminosities (upper panel of Fig. 7). But a steeper density slope reduces the radius  $R_{\text{em}}$  of the emitting region and results in higher surface density upper limits at 1 AU (middle panel of Fig. 7). For instance, the  $R_{\text{em}}$  for the [S I] line decreases from 10.4 AU for  $\alpha = 0.5$  to 3.7 AU for  $\alpha = 1.5$ , with the intermediate value of 5.5 AU for our fiducial disk (see Table 8). The  $\text{H}_2$  S(1) transition is more sensitive to the redistribution of mass than the [Fe II] and [S I] lines because it is the least optically thick transition. Differences between the limiting surface densities are less than a factor of 2 for  $\alpha$  differing by 0.5 (middle panel of Fig. 7). CO lines are not affected appreciably for  $\alpha = 1$  or larger but distributing more mass in the outer regions ( $\alpha = 0.5$ ) results in a more extended CO emission and therefore an increase of the mass associated with the emission (by a factor of 6). However, the outer disk mass between two fixed radii (in the zone 10–50 AU) differ by less than a factor of 2. Thus we conclude that uncertainties in the surface density slope introduce only a factor of a few uncertainty in our results.

We then consider the dependence of our results

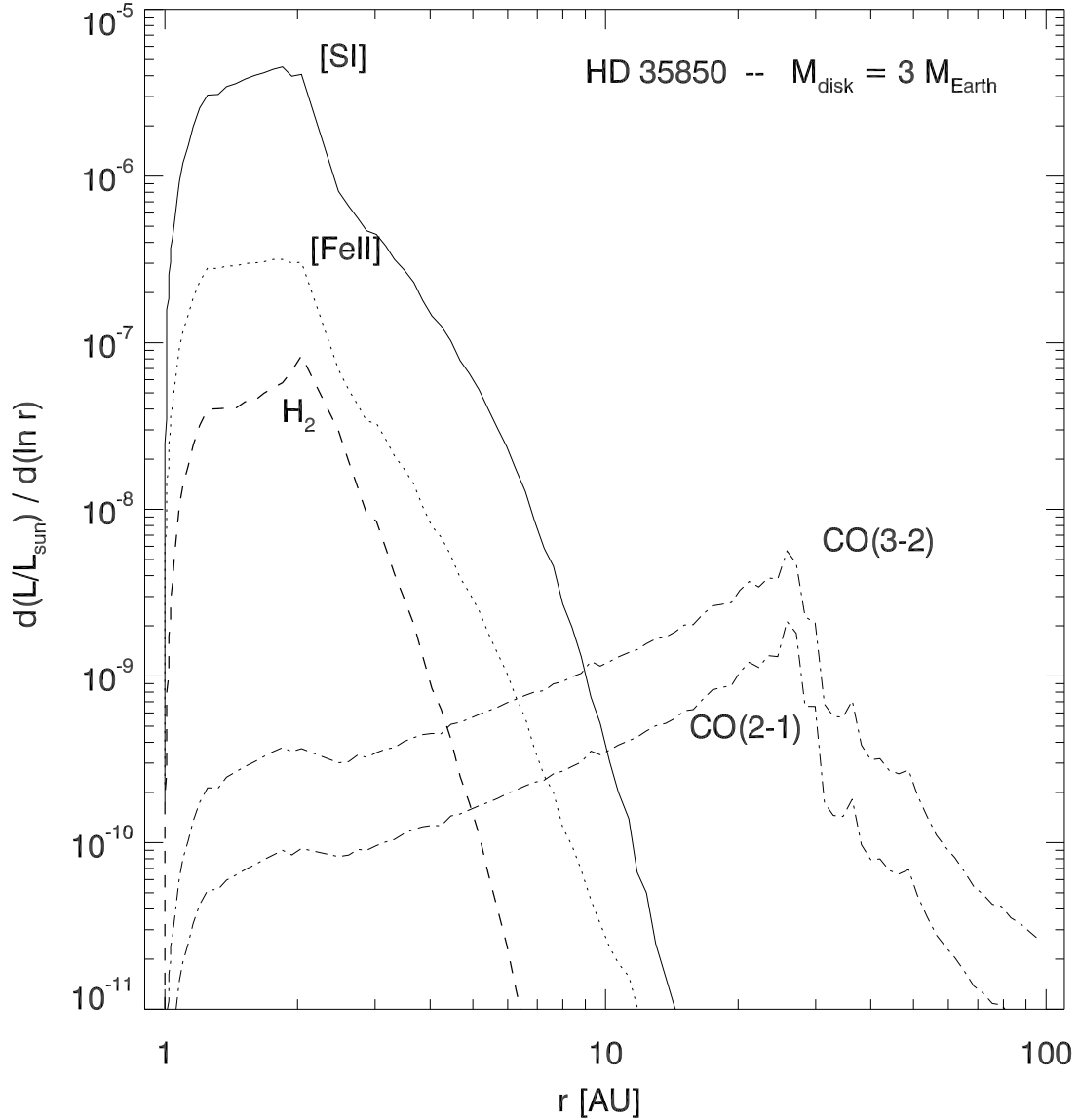


Fig. 6.— Emitting regions for mid-infrared and millimeter transitions. Plotted is the increment in line luminosity within a logarithmic radial annulus versus the disk radius. The luminosities of the  $\text{H}_2$  (dashed line),  $[\text{Fe II}]$  (dotted line), and  $[\text{S I}]$  (solid line) transitions steeply increase at the disk inner radius, remain high out to few AU, and rapidly decline at larger radii. The luminosities of millimeter CO transitions (dash-dotted lines) increase more gradually with radius. The drop in luminosity at  $\sim 30$  AU occurs because CO becomes optically thin to its own radiation at these radii and is rapidly photodissociated. The wiggles are due to the coarse grid spacing used for the calculation in the outer regions.

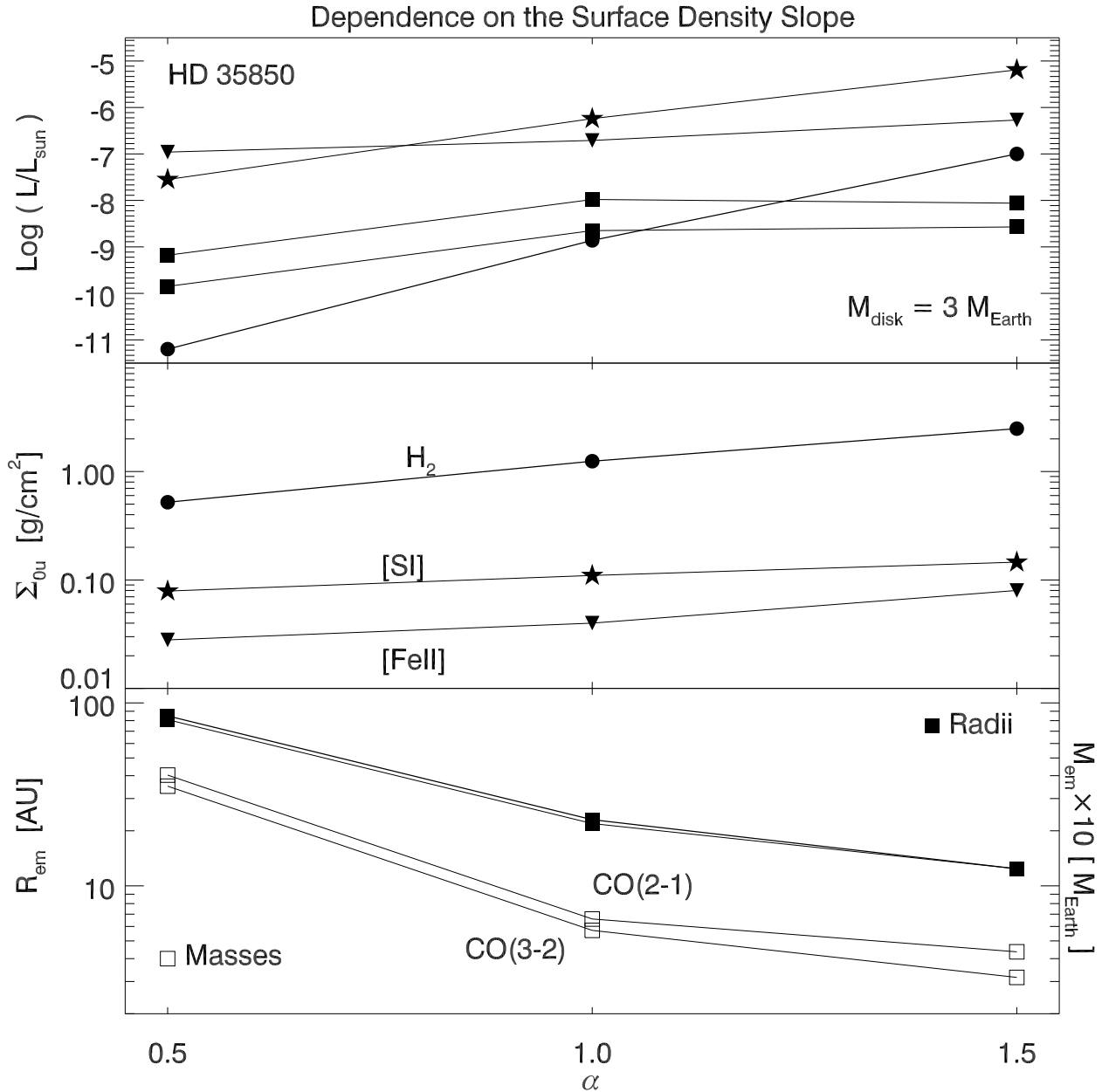


Fig. 7.— Dependence of our results on the surface density power law ( $\Sigma \propto r^{-\alpha}$ ). Changes in line luminosities for a disk of  $3M_{\oplus}$  around HD 35850 are plotted in the upper panel. Stars, upside down triangles, circles, and squares denote lines luminosities for the [S I], [Fe II],  $H_2$  S(1), and CO transitions respectively. The middle panel shows the variation in the surface density upper limits at 1 AU ( $\Sigma_{0u}$ ). Steeper density slopes ( $\alpha = 1.5$ ) increase the mid-infrared line luminosities and lower the total gas mass upper limits. However, the surface density at the inner radius also increases with alpha for a given disk mass, that's why the limits on the surface density are higher for  $\alpha = 1.5$  (see also text). The extension (filled squares) and mass (open squares) of the region emitting in the millimeter is plotted in the lower panel.



on different stellar UV luminosities. In addition to the UV flux for HD 35850 ( $G_0 = 7.37 \times 10^{10}$  at the stellar radius<sup>8</sup>) assumed previously, we have modeled two cases with 100 times higher and 100 times lower UV flux. The effect of higher stellar UV flux is to increase the heating (as well as alter the chemistry) and thus the predicted line luminosities of mid-infrared as well as of millimeter lines (see Fig. 8). Note that an increase of 4 orders of magnitude in the UV flux increases the mid-infrared and millimeter line luminosities by factors smaller than 20 and 3 respectively. Because our method provides order-of-magnitude estimates of the stellar UV field, model line luminosities have only a factor of a few uncertainty. Based on the previous tests on the surface density slope, such luminosity uncertainties should have negligible effects on the limiting surface densities and on the extension of the emitting regions (compare Figs. 7 and 8).

Finally, we test the dependence of our results on the disk inner radius. Our earlier modeling of HD 105 (H05) showed that, for a range of  $R_{\text{in}}$  between 1 AU and 40 AU, the upper limit on the surface density at the inner radius varied only by a factor of a few. This result is robust and can be extended to our sample: *Spitzer* data can set useful upper limits on the surface density for disks with  $R_{\text{in}}$  out to 40 AU<sup>9</sup>. For inner radii smaller than 1 AU, H05 found that the surface densities required to produce detectable lines increased (see their Fig. 6). This is because for smaller inner radii the mass or area (when lines are optically thick) of the emitting gas decreases. Essentially all the heating is deposited close to the star and gas located at larger radii becomes too cool to produce any line emission at mid-infrared wavelengths. The result was that if the disk inner radius of HD 105 became smaller than  $\sim 0.5$  AU, line upper limits from *Spitzer* could not set useful constraints on the gas mass.

In general, the sensitivity to the disk inner radius depends on the heating (stellar X-ray and UV) and on the line upper limits from *Spitzer*. While the younger sources in our sample typi-

<sup>8</sup> $G_0$  is the flux between 912-2000Å in units of  $1.6 \times 10^{-3} \text{ erg cm}^{-2} \text{ s}^{-1}$

<sup>9</sup>Note that  $R_{\text{em}}$  will change depending on  $R_{\text{in}}$ . The models from H05 suggest that the extension of the region where *Spitzer* lines originate is a few AU (see Table 2 from H05, there we used the notation  $r_w$  instead of  $R_{\text{em}}$ )

cally have higher X-ray and UV luminosities, and therefore produce more line flux, they are also more distant and so the upper limits on their luminosities are less stringent (see Fig. 9). To illustrate the effect of heating from stellar X-rays and UV we use the two disks around the F-type star HD 35850 and the K-type star HD 17925. We have chosen these sources because they represent extremes in stellar UV and X-ray luminosity (HD 35850 has high UV and X-ray luminosities, whereas HD 17925 has low UV and X-ray luminosities) and have IUE spectra and CO millimeter data (sources 12 and 14 in Fig. 9). We consider 5 disk models with inner disk radii equal to 1, 0.5, 0.3, 0.2, and 0.1 AU and compute for each case the surface density upper limits at the inner radius ( $\Sigma_0$ ) from the [S I] transition (filled symbols in Fig. 10)<sup>10</sup>. To show the effect of source distance, we also compute upper limits for HD 17925 at 30 pc ( $\text{Log}[L(\text{SI})/L_{\odot}] = -6.8$ ) and HD 35850 at 100 pc ( $\text{Log}[L(\text{SI})/L_{\odot}] = -5.5$ ), i.e. at about 3 times their real distance (open symbols in Fig. 10). To calculate these line luminosities we have assumed that the flux limits and the S/N do not change with the source distance and simply scaled the luminosities with the distance square (in reality our limits from the [S I] line are better for far-away sources due to longer exposure times but only by a factor of 4 at most). These tests show that: a) more distant sources will typically have larger  $\Sigma_0$  limits as well as larger disk inner radii at which the gas mass becomes unconstrained by *Spitzer* observations; b) high stellar heating lowers the limits on the gas surface density for sources at comparable distance (i.e., comparing HD 35850 at 27 pc and HD 17925 at 30 pc we see that we can set useful limits until  $R_{\text{in}} = 0.2$  AU for the more luminous HD 35850). Given the *Spitzer* upper limits and the stellar properties of our sample (Fig. 9), we conclude that we can set useful upper limits to the gas mass in the majority of our systems for disks with inner holes ranging from  $\sim 0.3$  to 40 AU. In the case of the more distant sources ScoPMS 214, MML 17, and MML 28, which are K- and G-type stars, the inner radius at which the surface density cannot be constrained may be larger than 0.3 AU but still less than 1 AU.

<sup>10</sup>We have also computed the  $R_{\text{em}}$  from CO lines and noted only marginal changes with  $R_{\text{in}}$

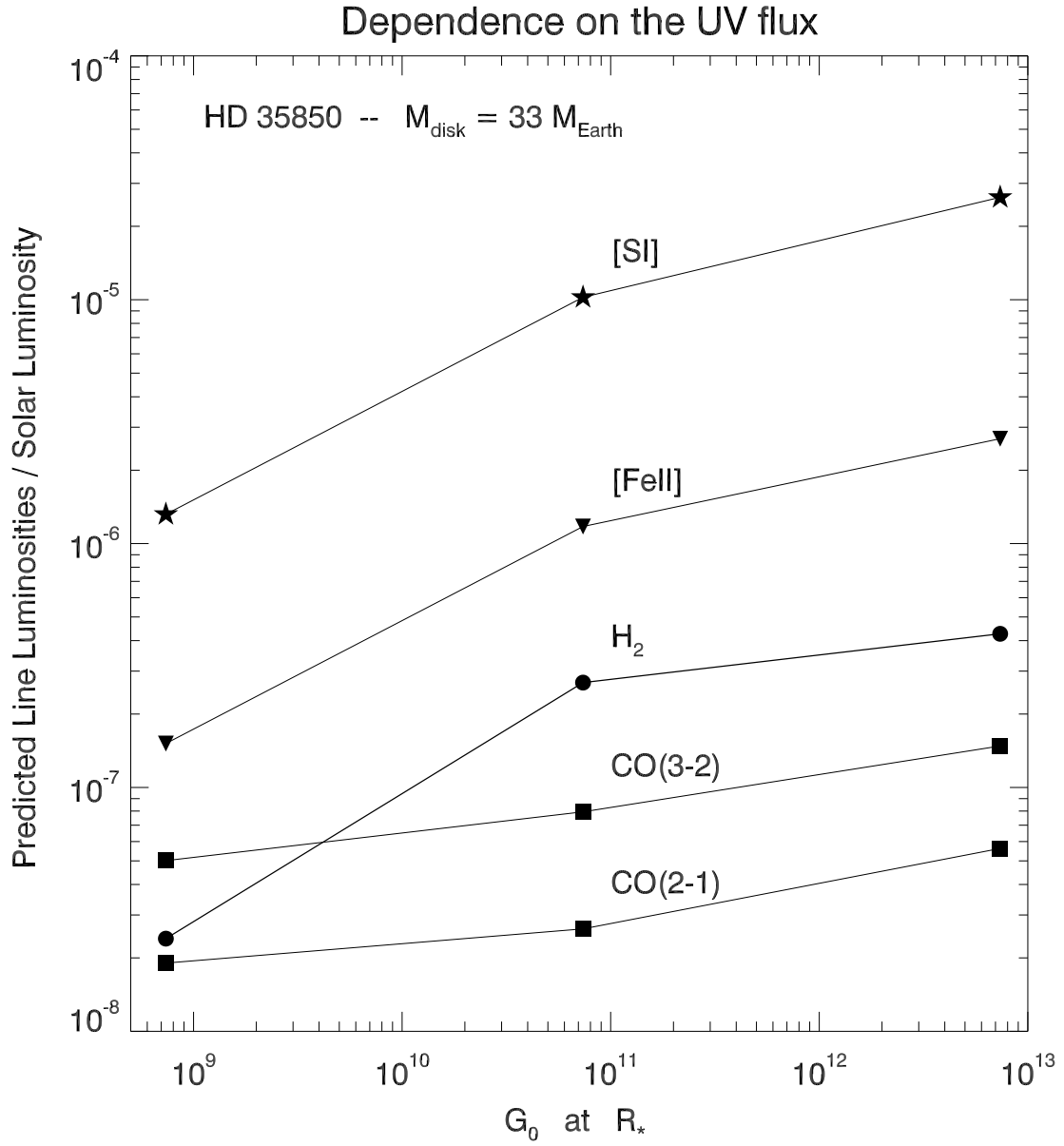


Fig. 8.— Dependence of line luminosities on the UV flux (see Fig. 7 for the symbols). These luminosities have been computed for a disk of  $33M_{\oplus}$  (from 1 to 100 AU) around the star HD 35850.  $G_0$  is the UV flux between 6 and 13.6 eV at the stellar surface normalized to the interstellar "Habing flux" ( $1.6 \times 10^{-3} \text{ erg cm}^{-2} \text{ s}^{-1}$ ).

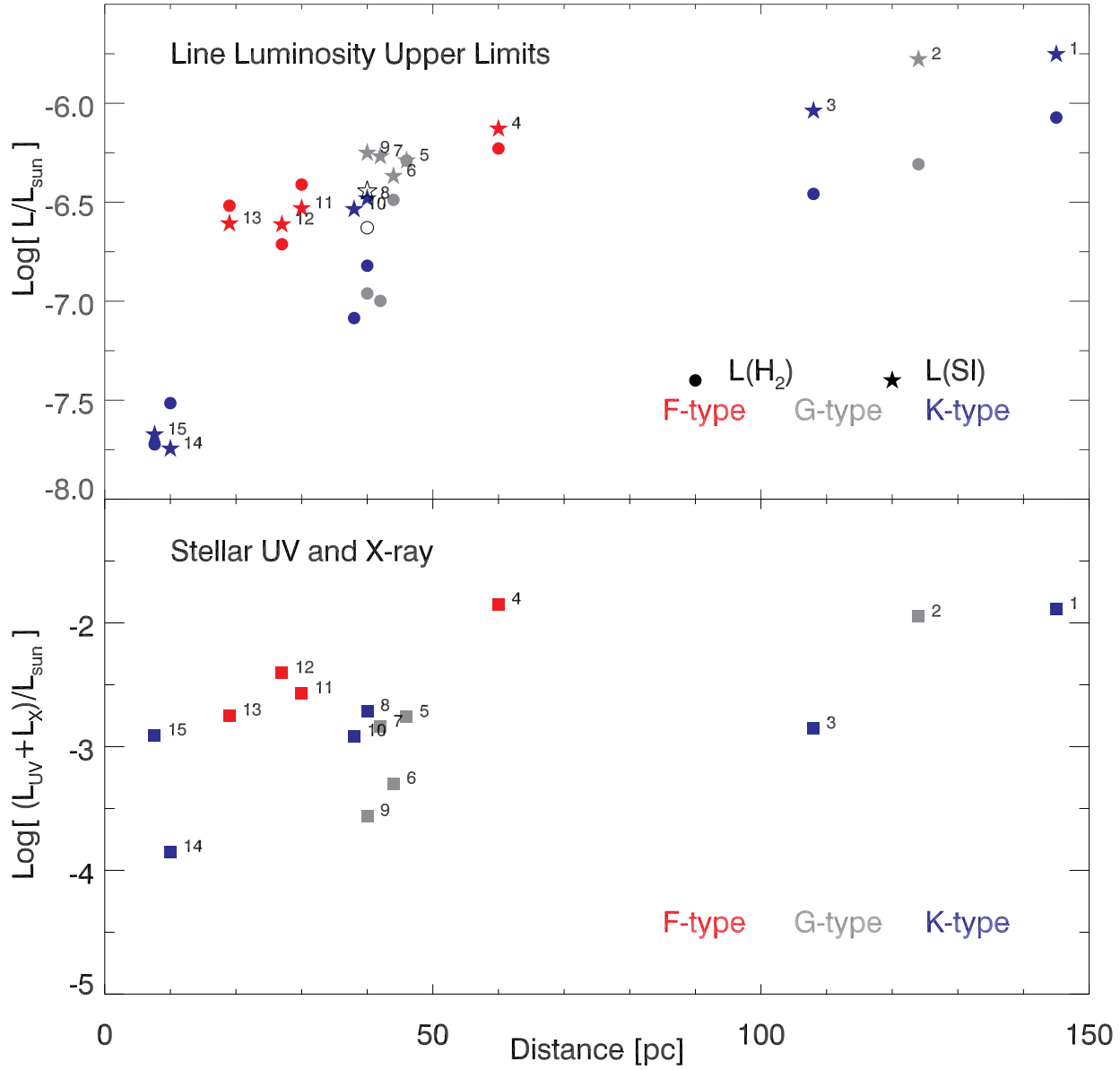


Fig. 9.— Upper panel. *Spitzer* line luminosity upper limits versus source distance. Stars and circles are for the [S I] and  $\text{H}_2$  S(1) transitions respectively. For comparison we report with open symbols the upper limits to HD 105 (H05). Symbols in red, gray, and blue indicate values from F-, G-, and K-type stars. Line luminosity limits are higher for the more distant sources. Lower Panel. Stellar UV and X-ray luminosities versus source distance. Early-type stars and young/more distant sources have higher luminosities.

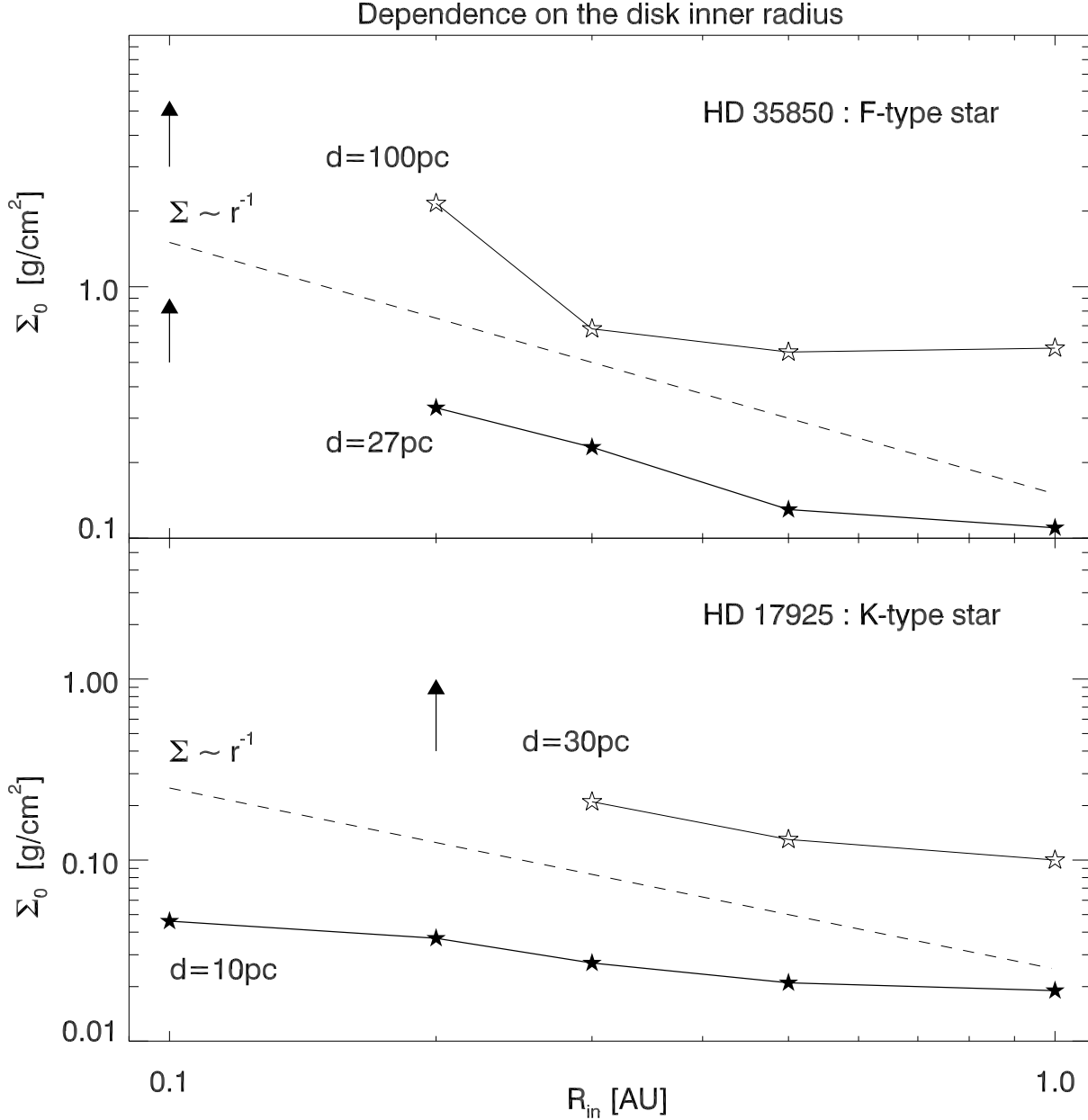


Fig. 10.— Dependence of the gas surface density upper limits ( $\Sigma_0$ ) on the disk inner radius.  $\Sigma_0$  is calculated from the upper limits to the [S I] line at the source distance (filled symbols) and at 30 pc and 100 pc for HD 17925 and HD 35850 respectively (open symbols). More distant sources have higher line luminosity upper limits that result in larger upper limits  $\Sigma_0$  and in larger  $R_{in}$  where the gas disk mass becomes unconstrained by *Spitzer* observations (this radius is marked by vertical arrows). For sources at a similar distance, upper limits to  $\Sigma_0$  are set by the stellar X-ray and UV fields and more constraining limits are obtained for disks around early-type stars (compare the results for HD 35850 at 27 pc and HD 17925 and 30 pc). The dashed line gives the dependence of our fiducial surface density with radius. The rise in  $\Sigma_0$  for  $R_{in} < 0.5$  AU is steeper than the fiducial surface density slope for the more distant sources, implying somewhat higher surface density upper limits at 1 AU for these disk inner radii.

## 5. Discussion

We have shown that infrared and millimeter observations set low limits to the amount of gas in the inner ( $\sim 1\text{-}5$  AU) and outer ( $\geq 15$  AU) regions, respectively, of our fiducial disks. In Sect. 4.3 we have proven that order-of-magnitude uncertainties in the stellar UV field and surface density slopes varying from  $-1.5$  to  $-0.5$  introduce only a factor of a few uncertainty in our results. Reducing the disk inner radius does not affect appreciably the result from the CO millimeter transitions because they originate farther out in the disk. On the other hand, mid-infrared lines are sensitive to small inner disk radii ( $< 1$  AU). Depending on the stellar properties, there is an inner radius at which *Spitzer* observations cannot set useful upper limits to the gas mass because the area or mass of the emitting gas is so small that lines cannot produce enough luminosity regardless of the surface density or the total disk mass. This critical inner radius is  $\lesssim 0.3$  AU for the majority of our targets, and between  $0.5$  and  $1$  AU for the three more distant systems (ScoPMS 214, MML 17, and MML 28). Thus the *Spitzer* observations alone can exclude the existence of gas disks with inner holes  $\gtrsim 0.3$  AU up to  $\sim 40$  AU around the nearby ( $d \leq 60$  pc) 12 targets and gas disks with inner holes  $\geq 1$  AU up to  $\sim 40$  AU around the 3 targets at distances larger than  $100$  pc.

We want now to convert surface density upper limits from the [S I] line, the most sensitive mid-infrared transition, to gas mass upper limits and answer the question of whether the targeted disks have enough gas at their present age to form gas giant planets. For  $R_{\text{in}} \gtrsim 1$  AU, we have shown in the previous Section that the [S I] line traces the inner few AU (with  $3$  AU being the mean value from Table 8) and provides very similar surface density upper limits at the disk inner radius. Thus, we can use the  $\Sigma_0$  at  $1$  AU in Table 8 as representative of the limiting gas surface density at the inner radius for disks with  $R_{\text{in}}$  between  $1$  and  $40$  AU. In this way, we find that *Spitzer* data can exclude gas masses larger than  $\sim 0.04 M_{\text{J}}$  within  $3$  AU of the inner radius for disks with inner radii between  $1$  and  $40$  AU.<sup>11</sup> This result is valid for all targets in

<sup>11</sup>These masses are not very sensitive to the assumed gas surface density slopes because of the small (few AU) region probed by mid-infrared gas lines.

our sample.

In addition, for the 12 nearby systems we can compute limits on the gas mass for disks with inner radii smaller than  $1$  AU. In the case of the nearby source HD 17925 (only  $10$  pc away) which has very stringent line flux upper limits, we can exclude gas disks with inner holes as small as  $0.1$  AU and a surface density at  $1$  AU even smaller than those reported in Table 8 (see Fig. 10). This result can be extended to HD 216803 which is similarly nearby and experiences even higher heating (Fig. 9). More generally, limits on  $\Sigma_0$  for  $R_{\text{in}} < 1$  AU increase faster than our assumed density slope and results in higher (up to a factor of  $10$  for  $R_{\text{in}}$  close to  $0.3$  AU) surface density upper limits than those reported in Table 8 (see Fig. 10 and the HD 105 models from H05). However, even if assume that  $\Sigma_0$  is  $20$  times larger at  $0.3$  AU (which gives  $5 \text{ g/cm}^2$ ), we find that there is less than  $0.0008 M_{\text{J}}$  of gas between  $0.3$  and  $1$  AU; a constant surface density slope would have resulted in less than  $0.002 M_{\text{J}}$  of gas.

But could we also rule out a substantial amount ( $\sim M_{\text{J}}$ ) of gas within  $1$  AU in the case of the three more distant systems? A gaseous disk extending close to the star may be accreting. We can use the upper limits on the stellar accretion rates for these sources to constrain the amount of gas in this disk region. The mass accretion rate of a steady  $\alpha$  disk around a solar-type star is<sup>12</sup>:

$$\dot{M} \simeq 7 \times 10^{-9} \left( \frac{\alpha}{0.01} \right) \left( \frac{T_{1\text{AU}}}{100\text{K}} \right) \left( \frac{\Sigma_{1\text{AU}}}{100 \text{ g/cm}^2} \right) [M_{\odot}/\text{yr}] \quad (2)$$

where  $\alpha$  is the viscosity parameter (typically  $0.01$  from magnetorotational instability models), and  $T_{1\text{AU}}$  and  $\Sigma_{1\text{AU}}$  are the gas disk temperature and the surface density at  $1$  AU. Accretion rates of  $\sim 10^{-8} M_{\odot}/\text{yr}$  are routinely measured in disks surrounding young ( $\sim 1$  Myr) classical T Tauri stars by modeling the UV excess emission and the profile of the  $\text{H}\alpha$  emission lines. Muzerolle et al. (2000) have extended these techniques to  $10$  Myr old stars in the TW Hya association and detected accretion rates down to  $\simeq 10^{-11} M_{\odot}/\text{yr}$  for lower

<sup>12</sup>Eq. 2 was derived from eq. 5.78, 5.64 and 5.31 from Hartmann (1998), assuming a gas surface density  $\Sigma \propto r^{-1}$  and the isothermal sound speed for a hydrogen gas. We normalize the temperature to  $100$  K because that is close to the dust temperature in the midplane of accreting T Tauri disks.

mass stars than are studied here. All our targets have been observed in H $\alpha$  with high spectral resolution and found to have only narrow H $\alpha$  lines (equivalent widths  $< 5 \text{ \AA}$ ) in absorption (White et al. 2006). The absence of H $\alpha$  in emission indicates that they have already passed the phase of active gas accretion. We can use the H $\alpha$  data for the three more distant sources and the minimum observable  $\dot{M}$  from magnetospheric accretion models to infer an upper limit to the mass accretion rate. Magnetospheric accretion models predict that the minimum observable  $\dot{M}$  depends on  $R_\star^{(3/2)} \times M_\star^{(1/2)}$  and is about  $10^{-10} M_\odot/\text{yr}$  for a 1 Myr old star with  $M_\star=0.5 M_\odot$  and  $R_\star=2 R_\odot$  (Muzerolle priv. comm.). Given this dependence, the absence of H $\alpha$  in emission and the radii and masses of the stars, we can conclude that residual accretion may persist in these disks only at low rates  $\lesssim 10^{-10} M_\odot/\text{yr}$ . Accretion rates  $\lesssim 10^{-10} M_\odot/\text{yr}$  translate into  $\Sigma_{1\text{AU}} \lesssim 1.4 \text{ g/cm}^2$  if the disk is accreting with  $\alpha = 0.01$  and  $T_{1\text{AU}}$  is 100 K (eq. 2). This surface density corresponds to a gas mass upper limit of  $0.001 M_J$  from the magnetospheric radius ( $3 R_\odot=0.01 \text{ AU}$ ) out to 1 AU when adopting our fiducial disk surface density of  $\Sigma \propto r^{-1}$ . Although  $\alpha = 0.01$  and  $T_{1\text{AU}}$  are extremely uncertain (and that’s why upper limits from *Spitzer* data alone are valuable), it seems very unlikely that even the three more distant systems have large amounts of gas within 1 AU. Surface density limits at 0.3 AU from the accretion are  $\lesssim 5 \text{ g/cm}^2$ , comparable to *Spitzer* limits for nearby sources but much more stringent than what could be set from infrared data alone on these three more distant sources.

In summary, we can exclude gaseous reservoirs of  $0.04 M_J$  within a few AU of the disk inner radius for disk radii from 1 AU up to  $\sim 40 \text{ AU}$ . *Spitzer* data alone are sensitive to small amounts of gas from about 0.3 AU to 1 AU for the majority of the sources. For the three more distant systems, accretion rate indicators set similarly stringent upper limits in the inner disk regions ( $< 1 \text{ AU}$ ). For disks with inner holes larger than 40 AU, mid-infrared transitions are not sensitive tracers of surface density because the gas is too cold. However, CO millimeter non-detections can exclude the presence of a large reservoir of cold gas at  $\geq 20 \text{ AU}$ . In conclusion, there is no indication that the targeted disks have enough gas to form Jupiter- or Saturn-like

planet(s). The present data cannot exclude the possibility that some or all of these systems have already formed such planets.

What can we learn about the gas dissipation timescale based on the above discussion? Our sample includes sources that are beyond the phase of active gas accretion. In addition, their small infrared excesses suggest that they have already dissipated most of their primordial dust and/or agglomerated it into larger particles. Our results show that by this time most of the gas has also been dispersed perhaps by photoevaporation (e.g. Clarke et al. 2001), and/or accreted to form gas giant planets. These conclusions are consistent with a rapid gas dissipation timescale that leaves little trace of gas in optically thin dust disks. More statistics on sources younger than 10 Myr in age and also on sources with optically thick dust disks are necessary to observationally constrain the gas lifetime and explore any link between gas and dust dissipation.

Short gas dissipation timescales are not only relevant to the formation of giant planets but also to the later stages of terrestrial planet formation. These final stages of growth may have involved tens to hundreds of planetary embryos over a timescale of 10 to 100 Myr (Canup 2004). Numerical simulations find that terrestrial planets grow to Earth-size in timescales of tens of million of years, in agreement with isotopic constraints (Kleine et al. 2002). A problem in the simulations of these later stages is that secular perturbations by (the presumably already formed) Jupiter and Saturn and by neighboring embryos excite terrestrial planet eccentricities<sup>13</sup>. Thus, some damping mechanisms seem to be required to circularize the final orbits of terrestrial planets. One possibility is through tidal interactions with a remnant gas disk. Kominami & Ida (2002) suggest that small amounts of gas, between 0.1– 0.01% of the minimum mass solar nebula (MMSN, Weidenschilling 1977; Hayashi 1981), can reduce the eccentricities to values as low as those of Earth and Venus on a timescale of about 10 Myr if secular perturbations from Jupiter and Saturn do not have a significant

<sup>13</sup>Collisions with large impactors (up to the mass of Mars) occur frequently at average times of  $\sim 30 \text{ Myr}$  and random orientations but seem to cause smaller changes in the eccentricities than secular perturbations (see e.g. Chambers 2001)

effect upon the evolution (Kominami & Ida 2004). Alternatively, dynamical friction associated with remnant swarms of planetesimals can damp the eccentricities over longer timescales even in the presence of perturbations from the giant planets (O’Brien et al. 2006; Raymond et al. 2006). Thus our low gas surface density upper limits at 1 AU (see Fig. 11) suggest that circularization of terrestrial planets if it occurs beyond 10 Myr may have happened primarily through the latter mechanism, although certainly gas could have played a role during the earlier stages of terrestrial planet formation.

Finally, the gas limits in the 10-40 AU region, the region mainly traced by our millimeter CO observations, may also be relevant to the formation of outer gas-poor giant planets such as Uranus and Neptune. Because of the dynamical interactions between embryos and the gravitational effects of Jupiter and Saturn, very little accretion of solids is expected to have occurred at the location of Uranus and Neptune in the absence of mechanisms to increase capture cross sections of embryos (Levison & Stewart 2001). One way to do this is through gas drag. However, this mechanism would require many Jupiter masses of gas (e.g. Goldreich et al. 2004) that are not observed in any of our targets (see Tables 8 and 9). The CO data for eight of our sources (with ages between 12 and few hundred Myr) indicate that less than 2 Earth masses of gas are present between 10 and 40 AU in our disks. These values are smaller than the gas mass of Uranus and Neptune as inferred by models of their interiors (Guillot 1999). Thus if Uranus and Neptune formed at their current radii, either gas persisted much longer in the solar nebula than was the case for our target stars, or they formed relatively quickly, in much less than 100 Myr.

## 6. Summary and Conclusions

We analyzed infrared and millimeter spectra for 15 of our FEPS sources selected for investigating the gas dispersal timescale in disks around solar-type stars. Our targets span a wide age range from 5 to few hundred Myr (with 50% of the sample younger than  $\sim 30$  Myr) and most are surrounded by optically thin dust disks. We did not detect gas lines in the *Spitzer* IRS modules nor in the millimeter with the SMT. We estimated upper limits

to the gas mass using simple approximations and also more sophisticated gas and dust models. In agreement with our previous modeling of HD 105 (H05), we find that optically thin dust disks have too little dust surface density to appreciably heat the gas. Therefore, X-ray and UV flux from the central star become the main heating mechanisms for the gas. We show that gas line upper limits from *Spitzer* provide sensitive limits to the gas surface density at the disk inner radius. Millimeter CO data are complementary by setting limits on the gas mass in the outer disk ( $\geq 15$  AU). We have also discussed the robustness of our results by varying the main uncertain input parameters to the disk models. Future work will include a study weighted towards disks younger than 10 Myr and tests of the gas models on sources with detected gas lines probing different disk regions. Our main conclusions can be summarized as follows:

1. Simple estimates of gas mass upper limits from mid-infrared H<sub>2</sub> lines indicate that even the five youngest disks (5-20 Myr) in our sample have less than  $0.6 M_J$  of gas at 100 K. Detailed gas models of the infrared and millimeter upper limits combined with the absence of accretion signatures allow us to conclude that none of the targeted disks have enough gas to form Jupiter- or Saturn-like planets at the present time.
2. Our results do not support the presence of "large quantities of gas in debris disks" as proposed by Thi et al. (2001a). On the contrary, we have evidence that systems with small dust excess in the 10-30 Myr age range do not have large amounts of remnant gas.
3. We estimate gas surface density upper limits at 1 AU smaller than 0.01% of the MMSN model for most of the sources, eight of which have ages between 5-30 Myr. If the circularization of terrestrial planets occurs in this age range, then gas surface densities appear to be so low that interactions with planetesimals seem to be the only viable mechanism to circularize their orbits.
4. The gas limits from CO data in the 10-40 AU region are less than a few  $M_{\oplus}$ . These values are far too low for gas drag to enhance the gravitational cross section of em-

## Gas Surface Density Upper Limits

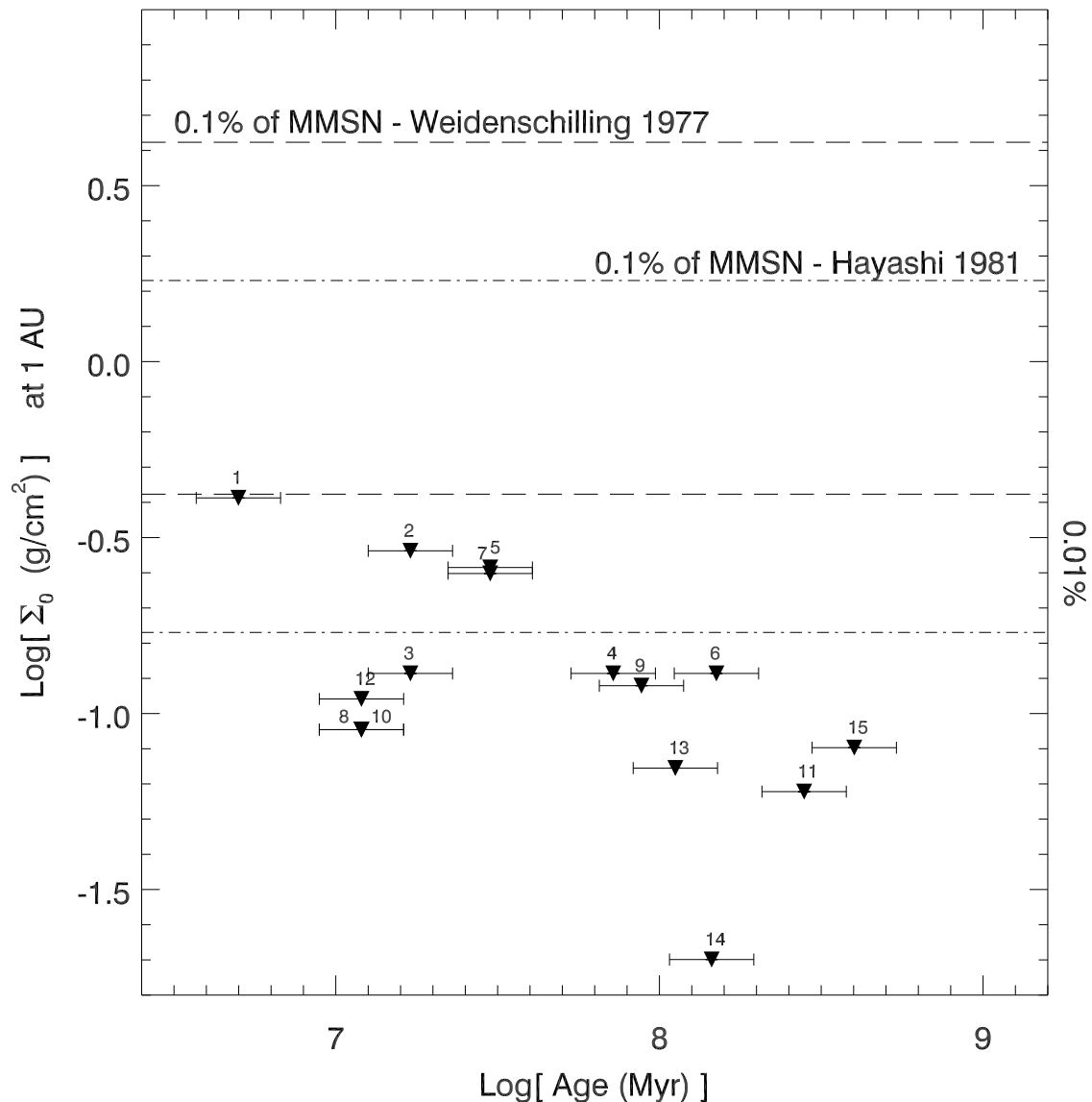


Fig. 11.— Gas surface density upper limits versus age compared to the surface density of the MMSN model from Weidenschilling (1977) (dashed lines) and from Hayashi (1981) (dash-dotted lines). Surface density upper limits are from the [S I] line for a disk with  $R_{\text{in}}=1$  AU (see Table 8), ages and errorbars are from Table 1. Our surface density upper limits at 1 AU are lower than 0.01% of the MMSN value from Weidenschilling (1977) for all sources. Note that the anti-correlation between the density upper limits at the inner radius and age does not depend on our model assumptions but rather on the properties of our sample. Because young sources are more distant than old ones, our line luminosity upper limits are less stringent for young disks (see Table 1 and Fig. 9).



bryos and speed up the in-situ formation of Uranus and Neptune. In addition, if these systems are analogs of the Solar System, our results indicate relatively short timescales ( $\ll 100$  Myr) for the formation of Uranus- and Neptune-like planets.

It is a pleasure to thank all members of the FEPS team for their contributions to the project and to this study. IP wishes to thank D. Watson for suggestions in the data reduction of the IRS high-resolution spectra and J. Muzerolle for helpful discussions on the mass accretion rate in young circumstellar disks. We would also like to thank the anonymous referee for a very careful and helpful review. This work is based on observations made with the Spitzer Space Telescope, which is operated by the Jet Propulsion Laboratory, California Institute of Technology under NASA contract 1407. Support for this work was provided by NASA through the FEPS Legacy award issued by JPL/Caltech.

Facilities: Spitzer Space Telescope.

## REFERENCES

- Apai, D., Pascucci, I., Bouwman, J., Natta, A., Henning, T., & Dullemond, C. P. 2005, *Science*, 310, 834
- Bary, J. S., Weintraub, D. A., & Kastner, J. H. 2003, *ApJ*, 586, 1136
- Bouwman, J., Meeus, G., de Koter, A., Hony, S., Dominik, C., & Waters, L. B. F. M. 2001, *A&A*, 375, 950
- Bryden, G., Beichman, C. A., Trilling, D. E., Rieke, G. H., Holmes, E. K., Lawler, S. M., Stapelfeldt, K. R., Werner, M. W., Gautier, T. N., Blaylock, M., Gordon, K. D., Stansberry, J. A., & Su, K. Y. L. 2006, *ApJ*, 636, 1098
- Buscombe, W. 1998, *VizieR Online Data Catalog*, 3206, 0
- Canup, R. M. 2004, *ARA&A*, 42, 441
- Chambers, J. E. 2001, *Icarus*, 152, 205
- Chen, C. H. 2005, to appear in the ASP conference proceedings of "Frank N. Bash Symposium 2005: New Horizons in Astronomy"
- Chen, C. H., Sargent, B. A., Bohac, C., Kim, K. H., Leibensperger, E., Jura, M., Najita, J., Forrest, W. J., Watson, D. M., Sloan, G. C., & Keller, L. D. 2006, *ArXiv Astrophysics e-prints*
- Chiang, E. I. & Goldreich, P. 1997, *ApJ*, 490, 368
- Clarke, C. J., Gendrin, A., & Sotomayor, M. 2001, *MNRAS*, 328, 485
- de Zeeuw, P. T., Hoogerwerf, R., de Bruijne, J. H. J., Brown, A. G. A., & Blaauw, A. 1999, *AJ*, 117, 354
- Dent, W. R. F., Greaves, J. S., & Coulson, I. M. 2005, *MNRAS*, 359, 663
- Draine, B. T. & Lee, H. M. 1984, *ApJ*, 285, 89
- Dutrey, A. & Guilloteau, S. 2004, *Ap&SS*, 292, 407
- Dutrey, A., Guilloteau, S., Duvert, G., Prato, L., Simon, M., Schuster, K., & Menard, F. 1996, *A&A*, 309, 493
- Dutrey, A., Lecavelier Des Etangs, A., & Augereau, J.-C. 2004, The observation of circumstellar disks: dust and gas components (Comets II), 81–95
- Fajardo-Acosta, S. B., Stencel, R. E., Backman, D. E., & Thakur, N. 1999, *ApJ*, 520, 215
- Gautier, D., Hersant, F., Mousis, O., & Lunine, J. I. 2001, *ApJ*, 550, L227
- Goldreich, P., Lithwick, Y., & Sari, R. 2004, *ARA&A*, 42, 549
- Gray, R. O., Corbally, C. J., Garrison, R. F., McFadden, M. T., Bubar, E. J., McGahee, C. E., O'Donoghue, A. A., & Knox, E. R. 2006, *ArXiv Astrophysics e-prints*
- Gray, R. O., Corbally, C. J., Garrison, R. F., McFadden, M. T., & Robinson, P. E. 2003, *AJ*, 126, 2048
- Guillot, T. 1999, *Science*, 286, 72
- Habing, H. J. 1969, *Bull. Astron. Inst. Netherlands*, 20, 177

- Habing, H. J., Dominik, C., Jourdain de Muizon, M., Laureijs, R. J., Kessler, M. F., Leech, K., Metcalfe, L., Salama, A., Siebenmorgen, R., Trams, N., & Bouchet, P. 2001, *A&A*, 365
- Hartmann, L. 1998, *Accretion Processes in Star Formation* (Accretion processes in star formation / Lee Hartmann. Cambridge, UK ; New York : Cambridge University Press, 1998. (Cambridge astrophysics series ; 32) ISBN 0521435072.)
- Hayashi, C. 1981, *Progress of Theoretical Physics Supplement*, 70, 35
- Herczeg, G. J., Linsky, J. L., Valenti, J. A., Johns-Krull, C. M., & Wood, B. E. 2002, *ApJ*, 572, 310
- Hollenbach, D., Gorti, U., Meyer, M., Kim, J. S., Morris, P., Najita, J., Pascucci, I., Carpenter, J., Rodmann, J., Brooke, T., Hillenbrand, L., Mamajek, E., Padgett, D., Soderblom, D., Wolf, S., & Lunine, J. 2005, *ApJ*, 631, 1180
- Houk, N. 1982, *CDS Catalogue*
- Houk, N. & Cowley, A. P. 1975, *CDS Catalogue*
- Houk, N. & Smith-Moore, M. 1988, *CDS Catalogue*
- Houk, N. & Swift, C. 1999, *CDS Catalogue*
- Huensch, M., Schmitt, J. H. M. M., & Voges, W. 1998, *A&AS*, 132, 155
- Jacobsen, S. B. 2005, *Annual Review of Earth and Planetary Sciences*, 33, 531
- Jaschek, M. 1978, *Bulletin d'Information du Centre de Donnees Stellaires*, 15, 121
- Jonkheid, B., Faas, F. G. A., van Zadelhoff, G.-J., & van Dishoeck, E. F. 2004, *A&A*, 428, 511
- Keller, L. P., Hony, S., Bradley, J. P., Molster, F. J., Waters, L. B. F. M., Bouwman, J., de Koter, A., Brownlee, D. E., Flynn, G. J., Henning, T., & Mutschke, H. 2002, *Nature*, 417, 148
- Kim, J. S., Hines, D. C., Backman, D. E., Hillenbrand, L. A., Meyer, M. R., Rodmann, J., Moro-Martín, A., Carpenter, J. M., Silverstone, M. D., Bouwman, J., Mamajek, E. E., Wolf, S., Malhotra, R., Pascucci, I., Najita, J., Padgett, D. L., Henning, T., Brooke, T. Y., Cohen, M., Strom, S. E., Stobie, E. B., Engelbracht, C. W., Gordon, K. D., Misselt, K., Morrison, J. E., Muzerolle, J., & Su, K. Y. L. 2005, *ApJ*, 632, 659
- Kleine, T., Münker, C., Mezger, K., & Palme, H. 2002, *Nature*, 418, 952
- Kominami, J. & Ida, S. 2002, *Icarus*, 157, 43
- . 2004, *Icarus*, 167, 231
- Lecavelier des Etangs, A., Vidal-Madjar, A., Roberge, A., Feldman, P. D., Deleuil, M., André, M., Blair, W. P., Bouret, J.-C., Désert, J.-M., Ferlet, R., Friedman, S., Hébrard, G., Lemoine, M., & Moos, H. W. 2001, *Nature*, 412, 706
- Levison, H. F. & Stewart, G. R. 2001, *Icarus*, 153, 224
- Makarov, V. V. 2003, *AJ*, 126, 1996
- Mamajek, E. E., Meyer, M. R., & Liebert, J. 2002, *AJ*, 124, 1670
- Mathis, J. S. 1990, *ARA&A*, 28, 37
- Meyer, M. R., Backman, D. E., Weinberger, A. J., & Wyatt, M. C. 2006, *Protostars and Planets V*, in press
- Micela, G., Favata, F., & Sciortino, S. 1997, *A&A*, 326, 221
- Moor, A., Abraham, P., Derekas, A., Kiss, C., Kiss, L. L., Apai, D., Grady, C., & Henning, T. 2006, *ArXiv Astrophysics e-prints*
- Muzerolle, J., Calvet, N., Briceño, C., Hartmann, L., & Hillenbrand, L. 2000, *ApJ*, 535, L47
- Najita, J., Carr, J. S., & Mathieu, R. D. 2003, *ApJ*, 589, 931
- Najita, J. & Williams, J. P. 2005, *ApJ*, 635, 625
- O'Brien, D. P., Morbidelli, A., & Levison, H. F. 2006, *Icarus*, in press
- Pascucci, I., Wolf, S., Steinacker, J., Dullemond, C. P., Henning, T., Niccolini, G., Woitke, P., & Lopez, B. 2004, *A&A*, 417, 793

- Perryman, M. A. C., Lindegren, L., Kovalevsky, J., Hoeg, E., Bastian, U., Bernacca, P. L., Crézé, M., Donati, F., Grenon, M., van Leeuwen, F., van der Marel, H., Mignard, F., Murray, C. A., Le Poole, R. S., Schrijver, H., Turon, C., Arenou, F., Froeschlé, M., & Petersen, C. S. 1997, *A&A*, 323, L49
- Pollack, J. B., Hollenbach, D., Beckwith, S., Simonelli, D. P., Roush, T., & Fong, W. 1994, *ApJ*, 421, 615
- Preibisch, T., Brown, A. G. A., Bridges, T., Guenther, E., & Zinnecker, H. 2002, *AJ*, 124, 404
- Przygodda, F., van Boekel, R., Àbrahàm, P., Melnikov, S. Y., Waters, L. B. F. M., & Leinert, C. 2003, *A&A*, 412, L43
- Raymond, S. N., Quinn, T., & Lunine, J. I. 2006, *Icarus*, in press
- Ribas, I., Guinan, E. F., Güdel, M., & Audard, M. 2005, *ApJ*, 622, 680
- Richter, M. J., Jaffe, D. T., Blake, G. A., & Lacy, J. H. 2002, *ApJ*, 572, L161
- Rieke, G. H., Su, K. Y. L., Stansberry, J. A., Trilling, D., Bryden, G., Muzerolle, J., White, B., Gorlova, N., Young, E. T., Beichman, C. A., Stapelfeldt, K. R., & Hines, D. C. 2005, *ApJ*, 620, 1010
- Roberge, A., Weinberger, A. J., Redfield, S., & Feldman, P. D. 2005, *ApJ*, 626, L105
- Sako, S., Yamashita, T., Kataza, H., Miyata, T., Okamoto, Y. K., Honda, M., Fujiyoshi, T., & Onaka, T. 2005, *ApJ*, 620, 347
- Savage, B. D. & Sembach, K. R. 1996, *ARA&A*, 34, 279
- Schmitt, J. H. M. M. & Liefke, C. 2004, *A&A*, 417, 651
- Scoville, N. Z., Sargent, A. I., Sanders, D. B., Claussen, M. J., Masson, C. R., Lo, K. Y., & Phillips, T. G. 1986, *ApJ*, 303, 416
- Sheret, I., Ramsay Howat, S. K., & Dent, W. R. F. 2003, *MNRAS*, 343, L65
- Shu, F. H., Adams, F. C., & Lizano, S. 1987, *ARA&A*, 25, 23
- Song, I., Zuckerman, B., & Bessell, M. S. 2003, *ApJ*, 599, 342
- Spangler, C., Sargent, A. I., Silverstone, M. D., Becklin, E. E., & Zuckerman, B. 2001, *ApJ*, 555, 932
- Sternberg, A. & Neufeld, D. A. 1999, *ApJ*, 516, 371
- Su, K. Y. L., Rieke, G. H., Misselt, K. A., Stansberry, J. A., Moro-Martin, A., Stapelfeldt, K. R., Werner, M. W., Trilling, D. E., Bendo, G. J., Gordon, K. D., Hines, D. C., Wyatt, M. C., Holland, W. S., Marengo, M., Megeath, S. T., & Fazio, G. G. 2005, *ApJ*, 628, 487
- Tagliaferri, G., Cutispoto, G., Pallavicini, R., Randich, S., & Pasquini, L. 1994, *A&A*, 285, 272
- Takeuchi, T. & Artymowicz, P. 2001, *ApJ*, 557, 990
- Thi, W. F., Blake, G. A., van Dishoeck, E. F., van Zadelhoff, G. J., Horn, J. M. M., Becklin, E. E., Mannings, V., Sargent, A. I., van den Ancker, M. E., & Natta, A. 2001a, *Nature*, 409, 60
- Thi, W. F., van Dishoeck, E. F., Blake, G. A., van Zadelhoff, G. J., Horn, J., Becklin, E. E., Mannings, V., Sargent, A. I., van den Ancker, M. E., Natta, A., & Kessler, J. 2001b, *ApJ*, 561, 1074
- Valenti, J. A., Fallon, A. A., & Johns-Krull, C. M. 2003, *ApJS*, 147, 305
- Valenti, J. A., Johns-Krull, C. M., & Linsky, J. L. 2000, *ApJS*, 129, 399
- Voges, W., Aschenbach, B., Boller, T., Bräuninger, H., Briel, U., Burkert, W., Dennerl, K., Englhauser, J., Gruber, R., Haberl, F., Hartner, G., Hasinger, G., Kürster, M., Pfeffermann, E., Pietsch, W., Predehl, P., Rosso, C., Schmitt, J. H. M. M., Trümper, J., & Zimmermann, H. U. 1999, *A&A*, 349, 389
- Walter, F. M., Herczeg, G., Brown, A., Ardila, D. R., Gahm, G. F., Johns-Krull, C. M., Lisauer, J. J., Simon, M., & Valenti, J. A. 2003, *AJ*, 126, 3076

- Walter, F. M., Vrba, F. J., Mathieu, R. D., Brown, A., & Myers, P. C. 1994, *AJ*, 107, 692
- Weidenschilling, S. J. 1977, *Ap&SS*, 51, 153
- White, R. J., Gabor, J., & Hillenbrand, L. A. 2006, *AJ*, submitted
- Wichmann, R., Schmitt, J. H. M. M., & Hubrig, S. 2003, *A&A*, 399, 983
- Wood, B. E., Redfield, S., Linsky, J. L., Müller, H.-R., & Zank, G. P. 2005, *ApJS*, 159, 118
- Wyatt, M. C., Dermott, S. F., Telesco, C. M., Fisher, R. S., Grogan, K., Holmes, E. K., & Piña, R. K. 1999, *ApJ*, 527, 918
- Zuckerman, B., Forveille, T., & Kastner, J. H. 1995, *Nature*, 373, 494
- Zuckerman, B. & Song, I. 2004, *ARA&A*, 42, 685
- Zuckerman, B., Song, I., Bessell, M. S., & Webb, R. A. 2001, *ApJ*, 562, L87
- Zuckerman, B. & Webb, R. A. 2000, *ApJ*, 535, 959

Table 1: Summary of the target stellar parameters. Targets are ordered by distance, from the farthest (ScoPMS 214) to the closest (HD 216803).

#	Source	RA [J2000]	DEC [J2000]	SpT	Age [Myr]	D [pc]	$T_{\text{eff}}$ [K]	$\text{Log}(L_{\star})$ [ $L_{\odot}$ ]	$\text{Log}(L_{\text{x}})$ [erg/s]
1	ScoPMS 214 <sup>a</sup>	16:29:49	-21:52:11.9	K0 <sup>(1)</sup>	5 <sup>b</sup>	145	5318	0.26	30.72 <sup>(11)</sup>
2	MML 17	12:22:33	-53:33:49.0	G0 <sup>(2)</sup>	17 <sup>c</sup>	124	6000	0.43	30.30 <sup>(2)</sup>
3	MML 28	13:01:51	-53:04:58.1	K2 <sup>(2)</sup>	17 <sup>c</sup>	108	4997	-0.35	30.00 <sup>(2)</sup>
4	HD 37484	05:37:40	-28:37:34.7	F3 <sup>(3)</sup>	72	60	6727	0.55	29.07 <sup>(12)</sup>
5	HD 202917	21:20:50	-53:02:03.1	G5 <sup>(4)</sup>	30 <sup>d</sup>	46	5553	-0.18	29.49 <sup>(13)</sup>
6	HD 134319 <sup>a</sup>	15:05:50	+64:02:50.0	G5 <sup>(5)</sup>	150	44	5716	-0.14	29.23 <sup>(11)</sup>
7	HD 12039	01:57:49	-21:54:05.3	G3/5 <sup>(6)</sup>	30 <sup>d</sup>	42	5688	-0.05	29.10 <sup>(13)</sup>
8	V343 Nor <sup>a</sup>	15:38:58	-57:42:27.3	K0 <sup>(4)</sup>	12 <sup>e</sup>	40	5103	-0.03	30.73 <sup>(11)</sup>
9	HD 377	00:08:26	+06:37:00.5	G2 <sup>(7)</sup>	88	40	5852	0.09	29.10 <sup>(11)</sup>
10	AO Men <sup>a</sup>	06:18:28	-72:02:41.6	K3 <sup>(8)</sup>	12 <sup>e</sup>	38	4359	-0.59	30.16 <sup>(14)</sup>
11	HD 209253	22:02:33	-32:08:01.6	F6/7 <sup>(3)</sup>	280	30	6217	0.21	29.70 <sup>(15)</sup>
12	HD 35850	05:27:05	-11:54:03.4	F7/8 <sup>(9)</sup>	12 <sup>e</sup>	27	6138	0.25	30.60 <sup>(13)</sup>
13	HD 25457	04:02:37	-00:16:08.2	F7 <sup>(10)</sup>	110	19	6319	0.32	29.74 <sup>(16)</sup>
14	HD 17925	02:52:32	-12:46:11.2	K1 <sup>(6)</sup>	150	10	5173	-0.43	28.97 <sup>(17)</sup>
15	HD 216803 <sup>a</sup>	22:56:24	-31:33:56.1	K4 <sup>(3)</sup>	400	7.6	4531	-0.71	28.34 <sup>(17)</sup>

NOTE.—Units of right ascension are hours, minutes, and seconds, and units of declination are degrees, arcminutes, and arcseconds. Spectral types are from optical spectroscopy with accuracy of 0.5 to 1 subtype (references in parenthesis). Column six reports the stellar ages: for members of stellar groups we report the mean group ages (see notes below), otherwise we report mean ages from Hillenbrand et al. (2006, in preparation). Typical errors are 30% of the adopted age. All distances, except for ScoPMS 214, are from Hipparcos (Perryman et al. 1997); we assume the mean distance to Upper Sco (de Zeeuw et al. 1999) for ScoPMS 214. Effective temperatures are mainly from B,V,K photometry while bolometric luminosities are from the best fit Kurucz stellar models to optical and near-infrared observations of the stellar photosphere (we refer to Carpenter et al. 2006, in preparation for the procedure). X-ray luminosities are reported in the last column of the table with references in parenthesis.

<sup>a</sup>These sources do not have excess emission at any of the observed wavelengths (see Sect. 2.1 for details)

<sup>b</sup>This source belongs to the Upper Scorpius group (Preibisch et al. 2002)

<sup>c</sup>These sources belong to the Lower Centaurus Crux association (Mamajek et al. 2002)

<sup>d</sup>These sources belong to the Tuc-Hor association (Zuckerman & Webb 2000; Song et al. 2003; Zuckerman & Song 2004; Moor et al. 2006)

<sup>e</sup>These sources belong to the  $\beta$  Pic moving group (Zuckerman et al. 2001; Zuckerman & Song 2004)

References. — <sup>(1)</sup> Walter et al. (1994); <sup>(2)</sup> Mamajek et al. (2002); <sup>(3)</sup> Houk (1982); <sup>(4)</sup> Houk & Cowley (1975); <sup>(5)</sup> Buscombe (1998); <sup>(6)</sup> Houk & Smith-Moore (1988); <sup>(7)</sup> Jaschek (1978); <sup>(8)</sup> Gray et al. (2006); <sup>(9)</sup> Houk & Swift (1999); <sup>(10)</sup> Gray et al. (2003); <sup>(11)</sup> Voges et al. (1999); <sup>(12)</sup> Micela et al. (1997); <sup>(13)</sup> Wichmann et al. (2003); <sup>(14)</sup> Makarov (2003); <sup>(15)</sup> Tagliaferri et al. (1994); <sup>(16)</sup> Huensch et al. (1998); <sup>(17)</sup> Schmitt & Liefke (2004);

Table 2: Log of the IRS high-resolution observations. The *RAMP* duration is the time in seconds per exposure. We acquired *ncycles* exposures before moving to the second slit position. The total on-source integration time is  $RAMP \times ncycles \times 2$ .

#	AOR Key	SH	LH
		$RAMP \times ncycles$	$RAMP \times ncycles$
ScoPMS 214	9776897	121.9×6	60.95×8
MML 17	13463296	121.9×6	60.95×6
MML 28	13462016	121.9×6	60.95×7
AO Men	5458688	121.9×2	60.95×2
HD 35850	9777920	31.46×6	14.68×10
V343 Nor	5458944	121.9×2	60.95×2
HD 12039	13461760	121.9×4	60.95×3
HD 202917	9778176	31.46×5	14.68×8
HD 25457	9779712	6.29×4	6.29×2
HD 37484	9780224	31.46×10	14.68×10
HD 377	13462272	121.9×3	60.95×3
HD 17925	9780480	31.46×5	14.68×8
HD 134319	9779968	31.46×6	14.68×10
HD 209253	9779200	31.46×7	14.68×4
HD 216803	9777664	31.46×5	14.68×8

Table 3: Millimeter observations and estimated 1-sigma upper limits (per channel) in K.

Source	$v_{\star}^a$	$\Delta T_{\text{rms}}$ [K]	
	[km/s]	CO(2-1)	CO(3-2)
ScoPMS 214	-7.6	0.033 <sup>I</sup>	0.18
HD 35850	20.2	0.043	0.083 <sup>I</sup>
HD 12039	3.1	0.049	0.078
HD 25457	17.6	0.028 <sup>I</sup>	0.044
HD 37484	23.7	0.038 <sup>I</sup>	–
HD 377	-4	0.043	0.13 <sup>I</sup>
HD 17925	17.7	0.042 <sup>I</sup>	0.056
HD 134319	-6.8	0.06 <sup>b</sup>	0.068 <sup>I</sup>
HD 209253	8.0	–	0.095 <sup>I</sup>

<sup>a</sup> $v_{\star}$  are the radial heliocentric velocities of the stars as measured by stellar spectroscopy (White et al. 2006). Errors on  $v_{\star}$  are about 0.5 km/s for all sources except for HD 377 where our uncertainty is 2 km/s.

<sup>b</sup>HD 134319 has been observed in the CO(2-1) transition by Najita & Williams using the heterodyne receiver at JCMT telescope (priv. communication, for the data reduction we refer to Najita & Williams 2005)

<sup>I</sup>Results from the first observational campaign (December-February 2003-2004).

Table 4: Line flux upper limits (5-sigma) from the high-resolution IRS spectra

Source	Log[Line flux (W/cm <sup>2</sup> )]					
	H <sub>2</sub> S(2)	H <sub>2</sub> S(1)	H <sub>2</sub> S(0)	[S I]	[Fe II]	[Si II]
ScoPMS 214	-21.73	-21.89	-21.41	-21.57	-21.57	-20.99
MML 17	-21.86	-21.99	-21.56	-21.46	-21.62	-20.95
MML 28	-21.95	-22.02	-21.51	-21.60	-20.27	-20.81
HD 37484	-21.13	-21.28	-21.20	-21.18	-21.36	-20.76
HD 202917	-21.10	-21.11	-21.15	-21.11	-21.34	-20.73
HD 134319	-21.18	-21.27	-21.17	-21.15	-21.28	-20.73
HD 12039	-21.60	-21.74	-21.29	-21.01	-21.42	-20.78
V343 Nor	-21.29	-21.52	-21.00	-21.18	-21.38	-20.60
HD 377	-21.45	-21.66	-21.33	-20.95	-21.12	-20.53
AO Men	-21.60	-21.74	-21.25	-21.19	-21.17	-20.87
HD 209253	-20.82	-20.86	-21.07	-20.98	-21.21	-20.51
HD 35850	-20.94	-21.07	-21.07	-20.97	-21.18	-20.75
HD 25457	-20.49	-20.57	-20.42	-20.66	-20.77	-20.11
HD 17925	-20.80	-21.01	-20.89	-21.24	-21.24	-20.64
HD 216803	-20.80	-20.98	-21.06	-20.93	-21.14	-20.68

Table 5: Gas mass upper limits estimated from the H<sub>2</sub> S(0) and H<sub>2</sub> S(1) non-detections for three gas temperatures. We used ortho-to-para ratios of 1.6, 2.5, and 3 for gas temperatures of 100, 150, and 200 K respectively (Sternberg & Neufeld 1999).

Source	H <sub>2</sub> mass [ $M_{\oplus}$ ]	Most sensitive line <sup>a</sup>
	for 100–150–200K gas	for 100K gas
ScoPMS 214	200–6.6–1.3	H <sub>2</sub> S(1)
MML 17	115–3.8–0.8	H <sub>2</sub> S(1)
MML 28	82–2.7–0.6	H <sub>2</sub> S(1)
HD 37484	64–4.6–0.9	H <sub>2</sub> S(0)
HD 202917	42–4.0–0.8	H <sub>2</sub> S(0)
HD 134319	37–2.5–0.5	H <sub>2</sub> S(0)
HD 12039	24–0.8–0.2	H <sub>2</sub> S(1)
V343 Nor	36–1.2–0.2	H <sub>2</sub> S(1)
HD 377	21–0.9–0.2	H <sub>2</sub> S(0)
AO Men	19–0.6–0.1	H <sub>2</sub> S(1)
HD 209253	22–3.1–0.6	H <sub>2</sub> S(0)
HD 35850	17–1.5–0.3	H <sub>2</sub> S(0)
HD 25457	39–2.4–0.5	H <sub>2</sub> S(1)
HD 17925	4–0.2–0.05	H <sub>2</sub> S(0)
HD 216803	1–0.1–0.03	H <sub>2</sub> S(0)

<sup>a</sup>For gas temperatures of 150 and 200 K the H<sub>2</sub> S(1) line is always more sensitive than the H<sub>2</sub> S(0) and the H<sub>2</sub> S(2) lines.

Table 6: Five-sigma upper limits for the line fluxes, CO masses, and outer disk radii.

Source	Log(Line flux) [W/cm <sup>2</sup> ]		$M_{\text{CO}}$ [ $M_{\oplus}$ ]		$R_{\text{out}}$ [AU]	
	CO(2-1)	CO(3-2)	CO(2-1)	CO(3-2)	CO(2-1)	CO(3-2)
ScoPMS 214	-23.43	-22.51	$1.2 \times 10^{-2}$	$3.1 \times 10^{-2}$	236	403
HD 37484	-23.37	–	$2.4 \times 10^{-3}$	–	105	–
HD 134319	-23.17	-22.93	$2.0 \times 10^{-3}$	$1.1 \times 10^{-3}$	97	75
HD 12039	-23.26	-22.87	$1.5 \times 10^{-3}$	$1.1 \times 10^{-3}$	83	77
HD 377	-23.32	-22.65	$1.2 \times 10^{-3}$	$1.7 \times 10^{-3}$	74	94
HD 209253	–	-22.79	–	$6.9 \times 10^{-4}$	–	61
HD 35850	-23.32	-22.85	$5.4 \times 10^{-4}$	$4.9 \times 10^{-4}$	50	51
HD 25457	-23.50	-23.12	$1.7 \times 10^{-4}$	$1.3 \times 10^{-4}$	28	26
HD 17925	-23.33	-23.02	$7.2 \times 10^{-5}$	$4.5 \times 10^{-5}$	18	15

NOTE.—CO masses are calculated assuming optically thin emission. The outer disk radii are estimated from the assumption of CO being optically thick. For both estimates we adopted a gas temperature of 20 K.



Table 7: Summary of UV luminosities and templates.

FEPS sources		UV templates			Ref.
Source	$\text{Log}(\frac{L_{\text{UV}}}{L_{\star}})$	Source	SpT	Criteria	
ScoPMS 214	-2.2	ScoPMS 52 <sup>a</sup>	K0IV	age, colors	1
MML 17	-2.4	HD 146516 <sup>a</sup>	G0IV	age, colors	1
MML 28	-2.6	ScoPMS 52 <sup>a</sup>	K0IV	age, colors	1
HD 37484	-2.4	HD 28568	F2V	X-ray	2
HD 202917	-2.6	HD 43162	G5V	X-ray	2
HD 134319	-3.2	HD 134319			3
HD 12039	-2.8	HD 43162	G5V	X-ray	2
V343 Nor	-3.3	V343 Nor			3
HD 377	-3.7	EK Dra	G1.5V	age, X-ray	4
AO Men	-2.5	RE J0137+18A	K3V	age, colors	3
HD 209253	-2.8	HD 33262	F7V	X-ray	2
HD 35850	-2.8	HD 35850			3
HD 25457	-3.1	HD 28033	F8V	X-ray	2
HD 17925	-3.5	HD 17925			3
HD 216803	-2.2	HD 216803			3

NOTE.—The UV luminosity we report here is calculated between 6.0 and 13.6 eV for comparison to the interstellar radiation field (Habing 1969).

<sup>a</sup>These two template stars belong to the Upper Scorpius association (d=145 pc) and have large visual extinctions as estimated from fitting their photometric data with Kurucz stellar atmospheres ( $A_V=1.5$  for ScoPMS 52 and  $A_V=0.8$  for HD 146516). Their IUE spectra have been deredden using the reddening law by Mathis (1990) before scaling them to the Kurucz model atmospheres of our targets. All other template stars have distances less than 65 pc and thus negligible extinction: their IUE spectra scaled to the source distances and radii were found to match well the source Kurucz model atmospheres at wavelengths longward of 3200 Å.

References. — 1. Valenti et al. (2000); 2. Wood et al. (2005) 3. IUE archive at <http://archive.stsci.edu/iue/>; 4. Ribas et al. (2005)

Table 8: Results derived from the Spitzer observations and the gas models.

Source	$\Sigma_0$ (g/cm <sup>2</sup> )			$R_{\text{em}}$ (AU)			$M_{\text{em}}$ ( $M_{\oplus}$ )			$M_{\text{disk}}$ ( $M_{\oplus}$ )
	H <sub>2</sub>	[Fe II]	[S I]	H <sub>2</sub>	[Fe II]	[S I]	H <sub>2</sub>	[Fe II]	[S I]	
ScoPMS 214	...	...	0.41	...	...	3.4	...	...	0.23	9.6
MML 17	...	...	0.29	...	...	2.9	...	...	0.13	6.8
MML 28	...	...	0.13	...	...	2.4	...	...	0.04	3.0
HD 37484	...	0.68	0.13	...	2.3	1.6	...	0.21	0.02	3.0
HD 202917	...	0.48	0.26	...	2.0	2.9	...	0.11	0.12	6.1
HD 134319	...	...	0.13	...	...	1.7	...	...	0.02	3.0
HD 12039	0.7	0.12	0.25	2.8	3.4	2.6	0.3	0.07	0.09	5.8
V343 Nor	...	0.05	0.09	...	4.6	5.1	...	0.04	0.09	2.1
HD 377	1.3	...	0.12	1.4	...	1.6	0.1	...	0.02	2.8
AO Men	0.9	0.13	0.09	4.2	2.7	3.3	0.7	0.05	0.05	2.1
HD 209253	...	0.29	0.06	...	1.8	2.5	...	0.06	0.02	1.4
HD 35850	1.2	0.04	0.11	2.5	4.2	5.5	0.4	0.03	0.12	2.6
HD 25457	...	0.41	0.07	...	1.7	2.9	...	0.07	0.03	1.6
HD 17925	...	0.36	0.02	...	1.4	1.8	...	0.03	0.004	0.5
HD 216803	0.3	0.07	0.08	2.5	1.5	1.9	0.1	0.008	0.02	1.9

NOTE.—Upper limits to the gas obtained from the line flux upper limits of H<sub>2</sub> at 17  $\mu\text{m}$ , [Fe II] at 26  $\mu\text{m}$ , and [S I] at 25.23  $\mu\text{m}$  and our fiducial disk model.  $\Sigma_0$  is the gas surface density at the disk inner radius (1 AU).  $R_{\text{em}}$  is the radius within which 90% of the emission originates.  $M_{\text{em}}$  is the gas mass between 1 AU and  $R_{\text{em}}$ . Total disk masses from the [S I] upper limits (last column) and our fiducial disk range from 0.5 (for HD 17925) to 8 (for ScoPMS 214)  $M_{\oplus}$ . However, note that they are not tightly constrained by the Spitzer observations alone, which are only sensitive to gas between the inner disk radius and  $R_{\text{em}}$ .

Table 9: Results derived from the SMT observations and the gas models.

Source	$R_{\text{em}}$ (AU)		$M_{\text{em}}$ ( $M_{\oplus}$ )		$R_{\text{thick}}$ (AU)		$M_{\text{disk}}$ ( $M_{\oplus}$ )
	CO(2-1)	CO(3-2)	CO(2-1)	CO(3-2)	CO(2-1)	CO(3-2)	CO(3-2)
ScoPMS 214	...	...	...	...	$> 100^{(100\%)}$	$> 100^{(100\%)}$	17
HD 37484	49.8	–	3.5	–	$50.1^{(90\%)}$	–	7.0
HD 134319	50.4	61.3	1.6	1.6	$43.5^{(87\%)}$	$43.5^{(83\%)}$	2.7
HD 12039	30.4	31.9	1.0	0.9	$20.5^{(62\%)}$	$19.6^{(56\%)}$	2.8
HD 377	36.4	53.8	1.2	2.3	$33.0^{(86\%)}$	$44.5^{(84\%)}$	4.4
HD 209253	–	31.1	–	0.7	–	$28.2^{(85\%)}$	2.6
HD 35850	23.0	21.9	0.7	0.6	$20.9^{(87\%)}$	$13.4^{(50\%)}$	2.7
HD 25457	28.4	26.4	0.5	0.4	$28.2^{(91\%)}$	$28.2^{(95\%)}$	1.5
HD 17925	21.1	20.1	0.07	0.05	$0^{(0\%)}$	$0^{(0\%)}$	0.3

NOTE.—Upper limits to the gas obtained from the SMT observations.  $R_{\text{em}}$  is the radius within which 90% of the emission originates.  $M_{\text{em}}$  is the mass between 1 AU and  $R_{\text{em}}$ . The CO(2-1) and CO(3-2) transitions trace colder gas in comparison to mid-infrared lines and thus are sensitive to the outer disk regions.  $R_{\text{thick}}$  is the radius at which the CO line optical depth is equal to 1, corresponding to a column density of CO molecules (perpendicular to the disk, along the vertical direction) approximately equal to  $10^{15} \text{ cm}^{-2}$ . The number in parenthesis gives the percentage of optically thick emission in comparison to the total CO emission. The last column gives the total disk (hydrogenic) masses from 1 to 100 AU for our fiducial disk surface density. These values are computed from the CO(3-2) transitions for all sources except ScoPMS 214 and HD 37484 where we used CO(2-1) data. In the case of ScoPMS 214 the CO(3-2) line flux upper limits are not stringent enough to set useful gas mass upper limits. For this gas mass the CO emission is optically thick all the way out to 100 AU. In the case of HD 37484 we have only CO(2-1) data